ACS Chemical Neuroscience

Research Article

pubs.acs.org/chemneuro

Molecular Dynamics Study on the Inhibition Mechanisms of Drugs CQ_{1-3} for Alzheimer Amyloid-β_{40} Aggregation Induced by Cu^{2+}

Mingyan Dong,[†] Haoyue Li,[‡] Dingkun Hu,[†] Wei Zhao,[†] Xueying Zhu,[†] and Hongqi Ai*[,†]

[†]School of Chemistry and Chemical Engineering, University of Jinan, Jinan 250022, China

[‡]Shandong Polymer Bio-chemical Co., Ltd., Dongying 257081, China

Supporting Information

ABSTRACT: The aggregation of amyloid-β (Aβ) peptide induced by Cu^{2+} is a key factor in development of Alzheimer's disease (AD), and metal ion chelation therapy enables treatment of AD. Three CQ_i (i = 1, 2, and 3 with R = H, Cl, and NO_2, respectively) drugs had been verified experimentally to be much stronger inhibitors than the pioneer clioquinol (CQ) in both disaggregation of Aβ_{40} aggregate and reduction of toxicity induced by Cu^{2+} binding at low pH. Due to the multiple morphologies of Cu^{2+}–Aβ_{40} complexes produced at different pH states, we performed a series of molecular dynamics simulations to explain the structural changes and morphology characteristics as well as intrinsic disaggregation mechanisms of three Cu^{2+}–Aβ_{40} models in the presence of any of the three CQ_i drugs at both low and high pH states. Three inhibition mechanisms for CQ_i were proposed as "insertion", "semi-insertion", and "surface" mechanisms, based on the morphologies of CQ_i–model x (CQ_i–x, x = 1, 2, and 3) and the strengths of binding between CQ_i and the corresponding model x. The insertion mechanism was characterized by the morphology with binding strength of more than 100 kJ/mol and by CQ_i being inserted or embedded into the hydrophobic cavity of model x. In those CQ_i–x morphologies with lower binding strength, CQ_i only attaches on the surface or inserts partly into Aβ peptide. Given the evidence that the binding strength is correlated positively with the effectiveness of drug to inhibit Aβ aggregation and thus to reduce toxicity, the data of binding strength presented here can provide a reference for one to screen drugs. From the point of view of binding strength, CQ_2 is the best drug. Because of the special role of Asp23 in both Aβ aggregation and stabilizing the Aβ fibril, the generation of a H-bond between CQ_3 and Asp23 of the Aβ_{40} peptide is believed to be responsible for CQ_3 having the strongest disaggregation capacity. Therefore, besides strong binding, stronger propensity to H-bond with Asp23 would be another key factor to be taken seriously into account in drug screens. Meanwhile, the structural characteristics of drug CQ_i itself are also worthy of attention. First, the increasing polarity from CQ_1 and CQ_2 to CQ_3 in turn results in increasing probability and strength of the interaction between the drug and the N-terminal (NT) region of Aβ_{40}, which obviously inhibits Aβ peptide aggregation induced by Cu^{2+} binding. Second, both the benzothiazole ring and phenol ring of CQ_i can overcome the activation energy barrier (~16 kJ/mol) to rotate flexibly around the intramolecular C7–N14 bond to achieve the maximum match and interaction with the ambient Aβ_{40} residues. Such a structural feature of CQ_i paves the new way for ones in selection and modification of a drug.

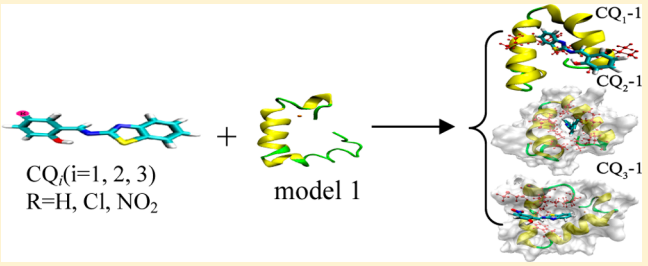

KEYWORDS: *Cu^{2+}–Aβ_{40} aggregation, CQ_i inhibitor, helix–coil/turn transition, insertion mechanism, rotation bond*

1. INTRODUCTION

Alzheimer's disease (AD) is the most common neurodegenerative disorder disease, characterized by fibrillar deposits of amyloid-β (Aβ) peptides and neurofibrillary tangles of Tau proteins.[1,2] Aβ peptides, varying from 39 to 43 residues, are produced from the Aβ precursor protein (APP). The predominant components of the senile plaques are 40 (Aβ_{40}) and 42 (Aβ_{42}) residue peptides, indicating that the misfolding and aggregation of the Aβ peptides are the chief causes of AD.[3] By comparison, Aβ_{40} is about 10 times more abundant than Aβ_{42} in vivo.[4]

Metal ions, Cu^{2+} and Zn^{2+}, are found in high concentration in the senile plaques[5] and can cause the configuration transformation of Aβ peptides and promote Aβ aggregation.[6,7] Earlier electron paramagnetic resonance (EPR) and nuclear magnetic resonance (NMR) experiments on Cu^{2+}/Aβ_{1-28} at physiological pH revealed a 3N1O coordination sphere, in which Cu^{2+} is coordinated by four ligands to form a square planar configuration, where 3N are the three N atoms {N^{H6}, N^{H13}, and N^{H14}} in iminazole rings of His6, His13, and His14, and 1O is one oxygen atom of a certain residue.[8] Using conventional continuous-wave (CW) EPR, the 1O was determined to be from the hydroxyl group of Ala2 by Drew et al.[9] Alí-Torres et al.[10] argued that the 1O derives from the Glu3 or Ala2 residue. When solvent effect is taken into account, the Ala2 is preferred. Otherwise, the oxygen from Glu3 would

Received: December 27, 2015
Accepted: February 12, 2016
Published: February 12, 2016

DOI: 10.1021/acschemneuro.5b00343
ACS Chem. Neurosci. 2016, 7, 599–614

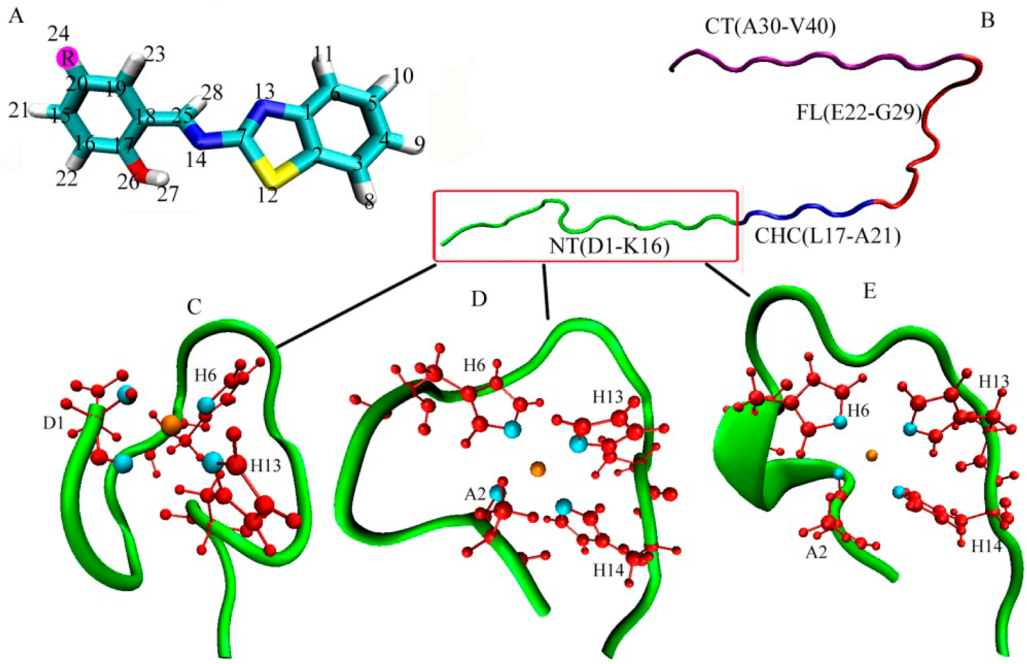

Figure 1. CQ_i (A), $A\beta_{40}$ monomer (B), and three coordinated modes (C, D, E) in model x (x = 1, 2, and 3). (A) Chemical structure of the CQ_i molecule, where i = 1, 2, and 3, corresponding to R = H, Cl, and NO_2, respectively. (B) Initial $A\beta_{40}$ monomers are from PDB 2LMN,[28] composed of four regions, NT (Asp1−Lys16), CHC (Leu17−Ala21), FL (Glu22−Gly29), and CT (Ala30−Val40). Mode C is generated at pH = 6−7 with coordination sites for Cu^{2+} of $\{O^{A1}, N^{D1}, N_{\delta}^{H6}, N_{\delta}^{H13}\}$. Modes D and E are produced at pH = 8−9, with the coordination sites for $Cu^{2+}$of $\{O^{A2}, N\varepsilon^{H6}, N\varepsilon^{H13}, N\varepsilon^{H14}\}$ and $\{O^{A2}, N\varepsilon^{H6}, N_{\delta}^{H13}, N\varepsilon^{H14}\}$, respectively.[13] The $A\beta_{40}$ monomer is shown in ribbon except for the residues coordinated by Cu^{2+} in ball and stick, where N atoms are highlighted in blue, O atoms in red, Cu^{2+} in orange, and R group in pink ball.

be more favorable to the stability of the 3N1O configuration.[10] In addition, the coordination sphere of Cu^{2+} in Cu^{2+}−Aβ strongly depends on solution pH. For instance, Drew et al. reported two coordination modes, **I** and **II**, of Cu^{2+}−Aβ, **I** $\{N^{D1}, O, N^{H6}, N^{H13/H14}\}$ at low pH and **II** $\{O, N^{H6}, N^{H13}, N^{H14}\}$ at high pH, where N^{D1} is the N from the terminal amino group of Asp1[11] instead of a histidine residue.[8−10] Combining previous work[9,11,12] and recent HM/QM simulation,[10] Alí-Torres et al.[13] summarized and further specified the two coordination modes of Cu^{2+}−Aβ at the two different pH ranges. They are modes **I** $\{O^{A2}, N^{D1}, N^{H6}, N^{H13}\}$ at low pH (pH = 6−7) and both **IIa** $\{O^{A2}, N^{H6}, N^{H13}, N^{H14}\}$ and **IIb** $\{O^{A2}, N^{A2}, N_{ter}, N^{H6}\}$ at high pH (pH = 8−9). Obviously, modes **I** and **IIa**/**b** characterize the main structures for Cu^{2+}−Aβ coordination under different acidic conditions. In a full-length $A\beta_{40}$ monomer, only the disorder residue sequence (N-terminal region, NT, Asp1−Lys16) (Figure 1) is the main region for Cu^{2+} to coordinate,[9−13] and yet the central hydrophobic region (CHC, Leu17−Ala21) and C-terminal region (CT, Ala30−Val40) are well-known as self-assembly regions, featuring the formation of stable β-sheets.[14] Between these two regions is their linker, the loop region (FL, Glu22−Gly29).

At present, there are three classes of common drugs to inhibit Aβ self-assembly. They are (1) peptide or peptide derivatives,[15] (2) chemical compounds extracted from natural products, and (3) synthetic compounds. For class 1, such as the fragment $A\beta_{16-20}$ (KLVFF) and its derivative LPFFD,[16] they break β-sheets and inhibit Aβ aggregation through hydrophobic interaction at the CHC region ($A\beta_{16-22}$). For class 2, such as (−)-epigallocatechin gallate (EGCG), a green tea extract,[17,18] they affect the transition of Aβ to fiber morphology by altering the conformation, increasing inter-center-of-mass distances, and reducing interchain contacts. The main binding sites (residues) are Phe4/Arg5, Tyr10, Phe19/Phe20, Gly29/Ala30/Ile31/Ile32, and Met35/Val36/Gly37/Gly38/Val39. For class 3, such as 1,4-naphthoquinon-2-yl-L-tryptophan (NQTrp),[19,20] they prefer to bind residues of Arg5, Asp7, Tyr10, His13, Lys16, Lys18, Phe19/Phe20, and Leu34/Met35.

Metal chelating agents are a common inhibitor for Aβ aggregation induced by metal ions. As one of the early clinical drugs to treat AD, clioquinol (CQ) can dissolve such aggregation by forming stable chelation with metal ions and consequently changing the concentration of free metal ions.[21] For example, CQ molecules can form a cage on the surface of Fe_3O_4 nanoparticles to prevent aggregation by sequestering copper after UV irradiation, and these conjugates can effectively inhibit Aβ aggregation and protect cells from Aβ-related toxicity upon light irradiation.[22] The drawback of CQ is its poor aqueous solubility and thus difficulty to enter the protein interior. Benzothiazole is known to possess strong binding affinity for β-amyloid plaques and has been used as an imaging agent for β-amyloid plaques.[23] Integrating the qualities of both CQ and benzothiazole, Geng et al.[24] synthesized three compounds, (*E*)-2-((benzo[*d*]-thiazol-2-ylimino)methyl)-phenol (CQ_1), (*E*)-2-((benzo[*d*]thiazol-2-ylimino)methyl)-4-chlorophenol (CQ_2),and (*E*)-2-((benzo[*d*]-thiazol-2-ylimino)-methyl)-4-nitrophenol (CQ_3), as new inhibitors of Cu^{2+}−Aβ aggregation, where CQ_i (i = 1, 2, and 3) is the collective term for them. The main difference in structure for the three CQ_i is the R group, where R = H (CQ_1), Cl (CQ_2), NO_2 (CQ_3) (shown in Figure 1). As small molecule derivatives, CQ_i can utilize the salicylaldehyde based Schiff base as the chelator of metal ion and benzothiazole[25] as the recognition moiety for AD treatment.

DOI: 10.1021/acschemneuro.5b00343
ACS Chem. Neurosci. 2016, 7, 599−614

Experiments had revealed that three CQ_i drugs exhibit high efficiency for both Cu^{2+} elimination and Aβ assembly inhibition[24] at pH = 6.6. Moreover, they can cross the blood−brain barrier[26] effectively, which fulfills drug-like criteria that are the most commonly defined using Lipinski's rules.[27] However, the mechanisms of both inhibition and disaggregation for such new drugs remain obscure. Due to the dependence of Cu^{2+}−Aβ aggregate morphologies on the solution pH, both the disaggregation ability and effect of the three CQ_i on high-pH Cu^{2+}−Aβ aggregates (i.e., in mode **II**) are unknown. Given this, we probed the interactions between three CQ_i drugs and Cu^{2+}−Aβ_{40} monomers obtained in the two pH ranges to disclose the inhibition effect and disaggregation mechanisms of the CQ_i as well as the associated dependence of configuration changes of Aβ_{40} peptide on the two different pH conditions, by which valuable clues for the discovery and design of new and effective inhibitors against the Aβ aggregation were provided.

2. MODELING AND COMPUTATIONAL METHODS

2.1. Modeling of Aβ_{40} Monomer and Cu^{2+}−Aβ_{40} Complexes. The full-length Aβ_{40} monomer was from the Aβ_{9-40} structure, PDB ID 2LMN,[28] completed by employing Chimera[29] to add the missing residue sequence of Asp1−Ser8. The three initial Cu^{2+}−Aβ_{40} structures were built by linking Aβ_{17-40} of 2LMN with Aβ_{16}−Cu^{2+}complexes of Alí-Torres's study[13] in mode **I** (Ia_$\delta\delta$) and **IIa** (including IIa_$\varepsilon\delta\varepsilon$ and IIa_$\varepsilon\varepsilon\varepsilon$) so that both acidity effect (by employing **Ia** and **IIa**) and computational simplification (by ignoring **IIb**) were taken into account. The Ia_$\delta\delta$ with coordination sites {O^{A1}, N^{D1}, N_δ^{H6}, N_δ^{H13}}was confirmed as the most stable mode **I** complex, and IIa_$\varepsilon\delta\varepsilon$, {$O^{A2}$, $N\varepsilon^{H6}$, N_δ^{H13}, $N\varepsilon^{H14}$} (with the thermal contributions), and IIa_$\varepsilon\varepsilon\varepsilon$, {$O^{A2}$, $N\varepsilon^{H6}$, $N\varepsilon^{H13}$, $N\varepsilon^{H14}$} (without the thermal contributions), were two most stable mode **IIa** complexes with only −0.7 kcal/mol difference in energy.[13] Herein these full-length Cu^{2+}−Aβ_{40} complexes are collectively referred to as model x (x = 1, 2, 3) in the following discussions.

To obtain parameters of these models x for the further MD, the following preparations were performed. First, smaller complexes, with Cu^{2+} centered and coordinated with four side chains of residues in modes of Ia_$\delta\delta$, IIa_$\varepsilon\delta\varepsilon$, and IIa_$\varepsilon\varepsilon\varepsilon$, were truncated from the Cu^{2+}−Aβ_{16} complexes,[13] in which each truncation bond linking the side chain and parental residue was saturated by H atom. Then optimization and frequency calculations were performed by utilizing the B3LYP/6-31G*[30,31] method to obtain the force constant parameters. Second, larger complexes were built by enlarging the smaller ones with entire residues included and capping the truncation bond of residues with NME and ACE, and then calculated to obtain point charge parameters based on the Merz−Kollman charge calculation. All these calculations were conducted by employing Gaussian03[32] software package. At last, these data were fitted by MTK ++/MCPB[33] module implemented in AmberTools12 to obtain the topology files, which were listed in Tables S1−S3 of the Supporting Information (SI).

2.2. Optimization and Parameterization for CQ_i. The chemical structures of three CQ_i were optimized at the B3LYP/6-31G* level by using Gaussian03.[32] Then Z-matrix optimizations were performed for these CQ_i complexes with rotating two rings from 0 to 180° along with the C7−N14 axis at the same level. The step was set as 10.0° with other parameters as variables correspondingly. Then the potential energy surface (PES) of CQ_i along with the dihedral angle change, N13−C7−N14−C25, could be obtained. To refine these results, M062X/6-31+G* optimizations were further performed because M062X method can describe noncovalent interactions in biomolecules better than current common-use density functionals.[34,35] The topology files of the three CQ_i molecules for the following MD simulations were created using the Antechamber program[36] in the Amber-tool 12.0 package and shown in Tables S4−S6 in SI.

2.3. Docking CQ_i to Cu^{2+}−Aβ_{40} Complex. Autodock4.1 package[37] was used to dock CQ_i to these full-length Cu^{2+}−Aβ_{40} peptides. The charges of both Cu^{2+} and coordination residues were manually changed by consulting the point charge parameters provided in section 2.1. Grid energies were calculated by using autogrid 4.0. The box dimension was set large enough to cover the entire receptor. Lamarckian genetic algorithm[38] was used for the docking operation, and the number of output was set to 100. The interaction effect between CQ_i and Cu^{2+}−Aβ_{40} was evaluated by the semiempirical free energy calculation method.[39] Because of the rigid docking between CQ_i and the Cu^{2+}−Aβ_{40} complex, any CQ_i molecules only locate on the surface of Aβ_{40} and thus generate poorer binding. It is obvious that such docked results would not reflect the real binding. Therefore, nine docking structures with the lowest binding energy were selected as the initial input files for further MD simulation, and they are termed as CQ_i−x for conciseness, where x denotes the xth model (model x). The energies and initial structures of these CQ_i−x are displayed in Table S7 and Figure S1 of SI, respectively. Figure S1 shows that the three drugs in CQ_i−1 mainly locate over the helical CHC regions with different structural orientations. The three drugs in the three initial CQ_i−2 however mainly locate over the junction of NT and CHC regions. CQ_2 and CQ_3 in the initial CQ_i−3 mainly locate near both the CHC and CT regions, whereas CQ_1 locates near the beginning of the CT region.

2.4. MD Simulation Methods. All MD simulations were performed using GROMACS-4.6 software package[40] with Amber94 force field. We chose Amber94 force field because it provides a better description of the structural and dynamic properties of well-structured proteins and allows folding of diverse proteins into their NMR structures.[41] Each system was immersed into a cubic box of TIP3P water with at least 8 Å distance around the solute, and an appropriate number of sodium counterions was added to maintain the electroneutrality. The van der Waals interactions were calculated using a cutoff of 1.0 nm. The nonbonded interaction pairlist, with a cutoff of 1 nm, was updated every 5 fs. The particle mesh Ewald method[42] was employed to treat the electrostatic interactions with a cutoff of 1.0 nm. The LINCS algorithm[43] was used to constrain the lengths of all covalent bonds to reduce the calculation time. The V-rescale temperature coupling[44] was used to control the temperature at 310 K. The Berendsen pressure coupling method[45] was applied to describe the barostat with constant pressure of 1 atm. All MD simulations were conducted using periodic boundary conditions. The simulation time was set from 50 to 500 ns, depending on the system equilibrium.

2.5. Analysis Tools and MM/PBSA Method. The root-mean-square deviation (RMSD) with the backbone atoms of protein was calculated using the g_rmsd in Gromacs. Secondary structure analysis was performed using the dictionary secondary structure of protein (DSSP) method.[46] The contact number of atoms was defined as the number of heavy atom pairs locating between CQ_i and model x with an interatomic distance of less than 6.0 Å.[47] The RMSD-based clustering method within a cutoff of 1.5 Å was used to generate the average protein structures, which can be presented in the figures by using the VMD program.[48]

The binding free energy (ΔG_b) between CQ_i and model x was estimated using the molecular mechanics/Poisson−Boltzmann surface area (MM/PBSA) method.[49,50] In detail, ΔG_b between a ligand (l) and a receptor (r) in a complex (c) was calculated as

$$\Delta G_b = G_c - (G_r + G_l) \quad (1)$$

where G_c, G_r, and G_l are the free energies of the complex (c), receptor (r), and ligand (l), respectively. G_c, G_r, and G_l can be further obtained by $G_y = E_{MM} - TS + G_s$ (y = c, r, l), where E_{MM} is the gas-phase energy, consisting of electrostatic (E_{elec}) and van der Waals (E_{vdw}) terms, and G_s is the sum of polar solvation energy (G_{GB}) and nonpolar solvation component (G_{np}). G_{GB} was calculated by the GB model.[51] G_{np} is from γSASA, where SASA (solvent-accessible surface area) was calculated using a water probe radius of 1.4 Å and γ was set to be 0.023 kJ/mol. The dielectric constants of the solute and solvent were set to 2 and 80, respectively. Because ΔG_b is a relative energy and the entropy estimate does not change significantly the relative affinity,[52] the

DOI: 10.1021/acschemneuro.5b00343
ACS Chem. Neurosci. 2016, 7, 599−614

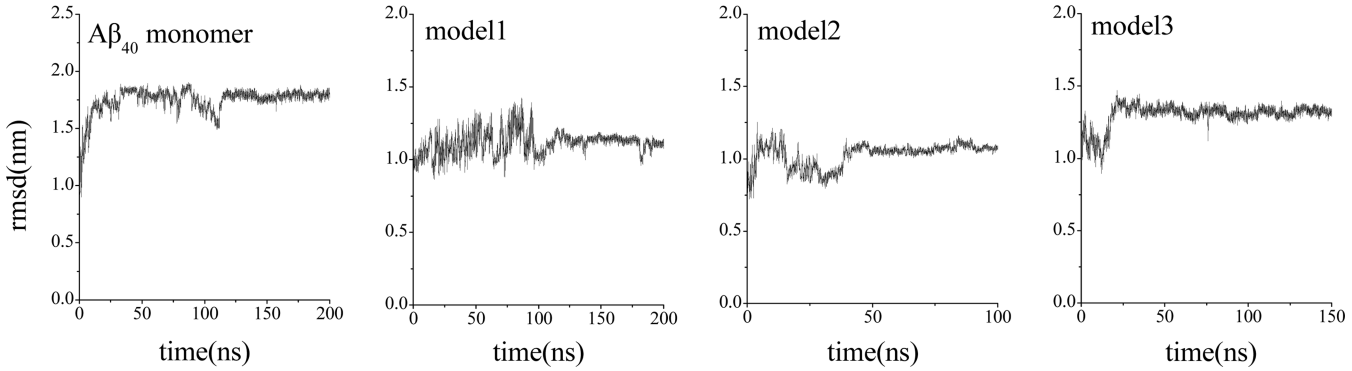

Figure 2. RMSDs of Aβ_{40} monomer and three models *x*.

contribution of conformational entropy of peptides can be ignored.[53] Then the practical calculation for ΔG_b was modified as $\Delta G_b = \Delta E_{MM} + \Delta G_s$.

3. RESULTS AND DISCUSSION

3.1. Aggregation Probability of Aβ_{40} Monomer Increases due to the Cu^{2+} Coordination. *3.1.1. Stability of Simulated Systems.* The RMSD results of Aβ_{40} monomer with or without Cu^{2+} bound at different pH states were shown in Figure 2. The system was assessed to be in equilibrium when the RMSD fluctuates around 0.1 nm. By this criterion, Figure 2 reveals that model 2 and model 3 reach the equilibrium states at about 50 ns, being faster than Aβ_{40} monomer and model 1 (ca. 120 ns), implying that the former two are more apt to achieve a stable structure. Furthermore, the three models *x* have smaller average RMSD values (1.1, 1.1, and 1.3 nm) during the plateaus than the Aβ_{40} monomer (1.8 nm), indicating that the binding of Cu^{2+} would increase the structural stability Aβ_{40} and as a result of increased aggregation of Aβ_{40}.

3.1.2. Binding Cu^{2+} Causes Great Changes of Aβ_{40} Monomer in Secondary Structure. A previous study revealed that β-sheet is the key factor to form protein folding,[54] whereas the conformational transition from α-helix to β-sheet is a crucial early step in Aβ amyloidogenesis.[55] Turn and coil structures are easier to transform into β-sheet ones due to their structural flexibility, whereas the helix structure must undergo three stages (S) of helix (S1) → coil/turn (S2) → β-sheet (S3) to convert into the β-sheet structure. The helix → coil strand transition features the exacerbation of variant toxicities,[54] indicating that the transition of S1→ S2 can be employed as a key index to probe the structure−property relationship for amyloid toxicity. Table 1 summarizes the probability of secondary structures, in which helix characterizes the structure of Aβ_{40} monomer, because the helix is the most populated (53%), and turn, coil and β-sheet structures hold populations of 36%, 10%, and zero, respectively. The result is reasonably consistent with that of two crystal structures, 1AML[56] (pH = 2.8) and 1BA4[57] (pH = 5.1), in which the helix component is also dominant. Structure 1AML contains two helix regions (residues Gln15−Lys23 and Ile31−Met35), whereas 1BA4 has one long helix composed of residues from Gln15 to Val36. Moreover, Viet et al's study[16] also observed the dominant helix component (45%) in the low energy structure of Aβ_{40} monomer by using Gromos 43a1 force field. Rojas et al.[58] confirmed using UNRES force field that Aβ_{40} monomer favors helix. The coarse-grained results[59] and CD estimated ones[60] argued that the α-helix content is at a lower level (~5%) however. Thus, what the intrinsic structure of monomer Aβ_{40} in an aqueous environment is requires further investigation.[16] Anyway, a comparison of the helix contents in Aβ_{40} monomer with those in Aβ_{40}−metal derivatives obtained by the same simulation method can avoid such errors originating from different measuring methods. In addition, a previous study[61] on the Aβ_{42} peptide revealed that the helix content also dominates the secondary structures of the Aβ_{42} monomer and has been employed to characterize successfully the conformation transition of Aβ_{42} peptide in the presence of inhibitors. Given this, we will probe the binding effect of Cu^{2+} and the inhibition effect of CQ_i by comparing the helix changes in the Aβ_{40} monomer with that in its Cu^{2+}−Aβ_{40} and CQ_i−Cu^{2+}−Aβ_{40} derivatives in the following discussions.

Table 1. Contents of Secondary Structures of Aβ_{40} Monomer, Model *x*, and CQ_i−*x*

systems	helix (%)	β-sheet (%)	turn (%)	coil (%)
Aβ_{40} monomer	53	0	36	10
model 1	41	0	42	17
model 2	28	0	52	20
model 3	25	2	42	30
CQ_1−1	67	0	21	12
CQ_1−2	41	0	38	19
CQ_1−3	27	0	43	29
CQ_2−1	66	0	23	11
CQ_2−2	37	0	44	19
CQ_2−3	30	0	45	25
CQ_3−1	59	0	31	10
CQ_3−2	37	0	43	16
CQ_3−3	35	0	37	24

Results revealed that the secondary structures of Aβ_{40} in the three models change greatly compared with that in the Aβ_{40} monomer, showing the effect of Cu^{2+} binding on the structures. In detail, the changes of secondary structure for model 1 are helix (−12%), coil (+7%)/turn (+6%), and β-sheet (0), where "+" means increase and "−" means decrease. As a result, coil and turn (59%) rather than the initial helix dominate the secondary structure in model 1, increasing the probability of Aβ_{40} aggregation and toxicity[62] upon Cu^{2+} binding. The changes of secondary structure in model 2 are helix (−25%), coil (+10%)/turn (+16%), and β-sheet (0), almost twice as much as that of model 1, indicating that the Cu^{2+}−Aβ_{40} coordination in model 2[13] is more favorable for aggregation and the resultant toxicity of Aβ_{40} than in model 1. By contrast, the population sum of coil (30%) and turn (42%) in model 3 is the same as that in model 2 (72%). The difference between them is that the feature structure of Aβ fibril, β-sheet content, emerges in model 3. Although the β-sheet content is slight

DOI: 10.1021/acschemneuro.5b00343
ACS Chem. Neurosci. 2016, 7, 599−614

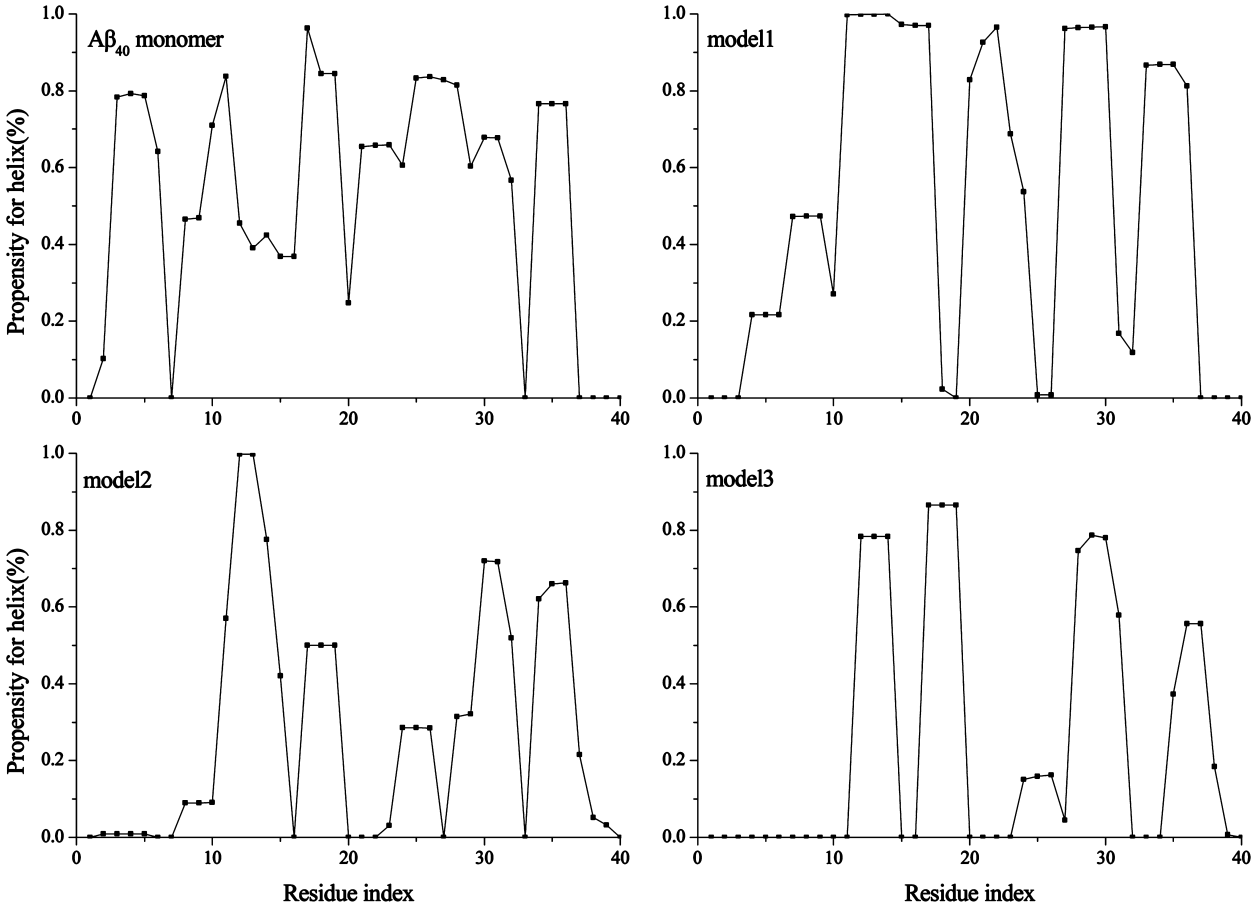

Figure 3. Probablities of helix in Aβ_{40} monomer and models *x*.

(2%) in model 3, it might serve as a key seed[63] or template[64] for further aggregation. Hence, the ability of Aβ_{40} aggregation induced by $Cu^{2+}$was predicted as follows: model 1 < model 2 < model 3.

Figure 3 partitions the contribution of each residue to the helix structure of Aβ_{40} and shows that the main contribution to helix structure in Aβ_{40} monomer focuses on both Glu3−His6 and Tyr10−Glu11 sequences in the NT region, Lys17−Phe19 in the CHC region, and the whole FL region, as well as Gly29−Ile32 and Leu34−Val36 sequences in CT region. This implies that the contribution of residues in the range of Gln15−Val36 sequence accounts for 75% of the entire helix region, resembling that in 1BA4.[57] Structure 1BA4 was resolved in an environment with pH = 5.1,[16] closer to the pH of water employed in the present paper. Khandogin and Brooks's experiment[54] confirmed that the helix propensity within the pH = 5.0−7.0 changes less although the helix formation of Aβ_{40} is pH-dependent. Therefore, the present prediction for helix contribution is consistent reasonably with that of 1BA4.

Compared with the helix population in Aβ_{40}, the population in Cu^{2+}−Aβ_{40} complexes changes greatly, manifesting stronger effect of metal ion coordination on the structure of Aβ_{40} (Figure S2). More specifically, the original helix contents composed of Glu3−His6 and Tyr10−Glu11 residue sequences in NT region of Aβ_{40} disappear and transform into turn content when mode 1 is generated. Meanwhile new helix composed of Glu11−Leu17 sequence emerges to accommodate the {N^{D1}, O^{D1}, N_{δ}^{H6}, N_{δ}^{H13}} coordination mode.[13] In the mode 1, there are four residues in the NT region involved in the chelation with Cu^{2+}, resulting in the former 10 residues being transformed into coil or turn structures, and only Phe20−Val24 in CHC and Asn27−Ala30 in FL region are in helix structure. Obviously, the helix contents in both CHC and FL regions are far less than that (Ala21−Ile32) in the Aβ_{40} monomer. Likewise, there is no helix structure in the former 10 residues in model 2, and the helix content in both CHC and FL regions reduces to Ala30−Ile32 from the original Ala21−Ile32 sequence of Aβ_{40} monomer. The helix distribution in model 3 is similar to that in model 2. If Cu^{2+}−Aβ_{40} coordination is in model 3, then the helix content of both Glu3−His6 and Tyr10−Glu11 of the NT region in Aβ_{40} disappears, but a new short helix occurs in Val12−His14 residues. Meanwhile, the original helix structures of Ala21−Ile32 in both CHC and FL regions of Aβ_{40} degenerate into Lys28−Ile32, and the helix of Leu34−Val36 in CT region turns into Val36−Gly37. Obviously, Cu^{2+} binding in any a model can decrease helix content in NT region of Aβ_{40} and transform most of it into turn or coil content (S2), heralding the increased toxicity[62] and high probability to transform into S3. The detailed comparisons for populations of coil and turn contents in Aβ_{40} with that in three model *x* complexes are shown in Figures S3 and S4, respectively.

3.2. CQ_i Drugs Can Recover the Secondary Structure of Aβ_{40} in Models *x*.

3.2.1. Contact between CQ_i and Model x. The stability of CQ_i−*x* systems can be monitored by assessing the total number of interatomic contacts between CQ_i and a model *x*. A system can be taken as reaching a dynamic equilibrium if the contact number is in a relatively stable state.[65]

DOI: 10.1021/acschemneuro.5b00343
ACS Chem. Neurosci. 2016, 7, 599−614

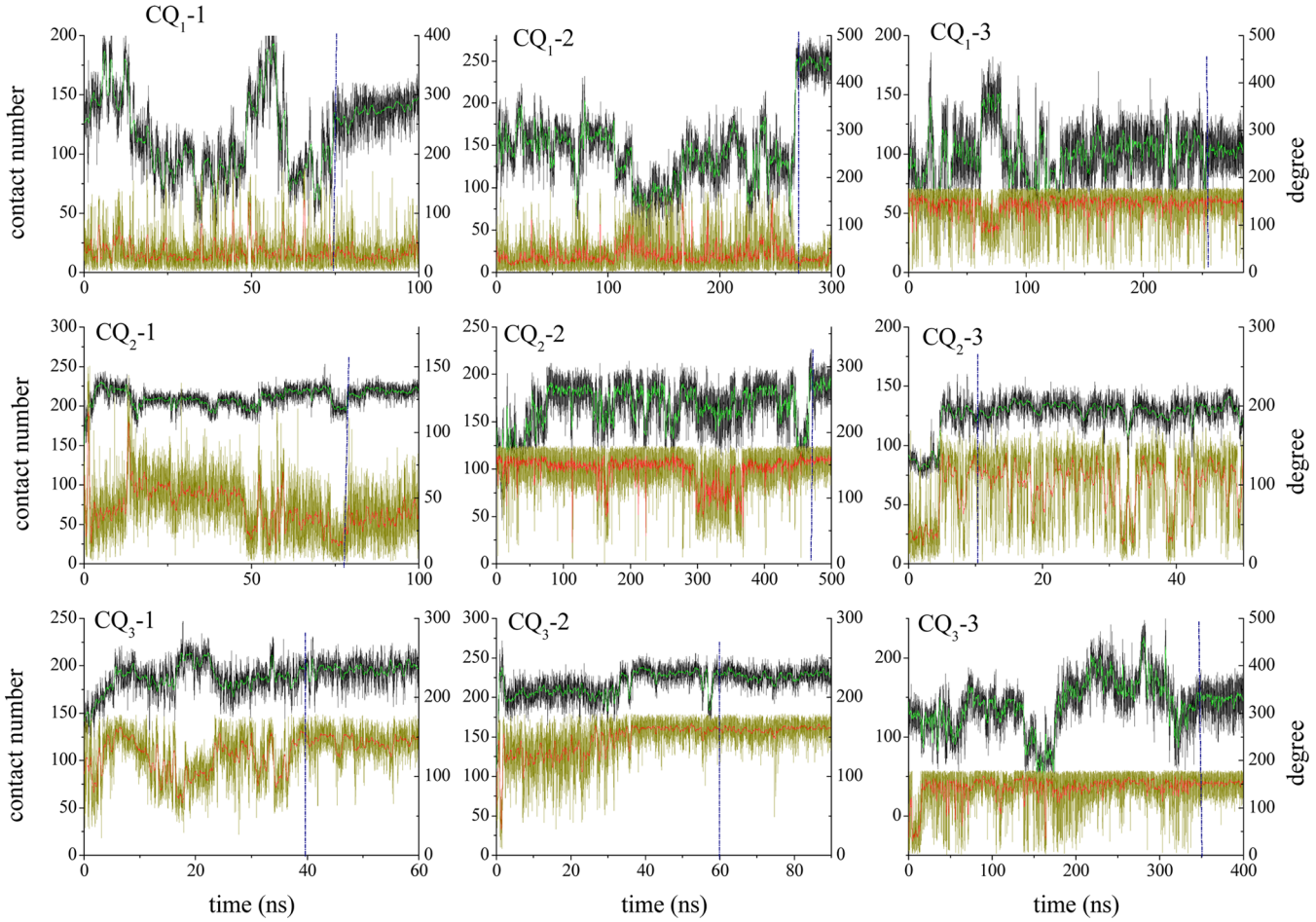

Figure 4. Intermolecular contact number (in black) marked on the left ordinate axis, which is defined as the number of heavy atom pairs located between CQ_i and model x with an interatomic distance of less than 6.0 Å, and the rotated dihedral angles (in olive) between phenol and benzothiazole rings of CQ_i marked on right ordinate axis. The fitted curves are highlighted in green and red, respectively. Blue dotted line indicates when the equilibrium is achieved for the CQ_i–x.

Figure 4 shows that the contact numbers between the identical drug and models 1, 2, or 3 are different. For example, the total contact numbers between CQ_1 and the three models x vary widely, from ∼136 in CQ_1–1 and ∼247 in CQ_1–2 to ∼102 in CQ_1–3, indicating different binding modes and strengths. The equilibrium time for three systems also differs widely, from 80 ns (CQ_1–1) and 250 ns (CQ_1–3) to 270 ns (CQ_1–2) (see dotted perpendicular lines marked in Figure 4), suggesting distinct dynamic processes for CQ_1 to contact the three models. The different contact numbers between CQ_2/CQ_3 and the three models x are as follows: CQ_2–1 (218) > CQ_2–2 (188) > CQ_2–3 (130) and CQ_3–2 > CQ_3–1 > CQ_3–3.

The atomic numbers of contact between any a CQ_i and the identical model x are also different. A comparison showed that the number ranking is 218 (CQ_2–1) > 196 (CQ_3–1) > 136 (CQ_1–1) for model 1, revealing the strongest binding strength in CQ_2–1. The number ranking of contact between CQ_i and model 2 is 247 (CQ_1–2) > 227 (CQ_3–2) > 188 (CQ_2–2), suggesting that CQ_1 has stronger contact with model 2. The number ranking of contact between CQ_i and model 3 is 148 (CQ_1–3) > 130 (CQ_2–3) > 102 (CQ_3–3). Obviously, the three contact numbers are smaller than their counterparts in CQ_1–x, indicating that three CQ_i drugs have a weaker ability to interact with model 3. In principle, atomic contact number has a positive correlation with the ability to bind between CQ_i and model x. A strong binding ability between drug and Aβ was suggested to be beneficial to prevent Aβ aggregation and concomitant neurotoxicity.[66]

3.2.2. CQ_i Recovery Effect on the Aβ Secondary Structure in Model x. 3.2.2.1. Helix of Model x Recovered by the Identical Drug. 3.2.2.1.1. Efficacy of CQ_1. Table 1 shows that secondary structure in CQ_1–1 changes greatly with 26% helix increase and 21% turn and 5% coil decrease, compared with those in model 1. The contents of secondary structure of CQ_1–1 become 67% S1 and 33% S2, indicating more helix population than that in Aβ_{40} monomer. This result discloses the stronger efficacy of CQ_1 for helix recovery, resulting in the highest population of helix content in model 1. The secondary structure in CQ_1–2 shows helix increase (+13%), turn decrease (−14%) and coil increase (+1%), compared with the counterparts in model 2, implying that CQ_1 indeed increases helix content and decreases turn, and the increased content of helix is almost equal to the decreased turn. In CQ_1–3, the changes of secondary structure are β-sheet (−2%) and helix (+2%), indicating that β-sheet content in the original model 3 disappears and converts into helix content. In all, the proportion of helix reduced by chelating with Cu^{2+} recovers greatly after the CQ_1 addition to the models x. The effect of the CQ_1 on the three models x is different, in which recovery in model 1 is the most remarkable with 26% helix recovery,

DOI: 10.1021/acschemneuro.5b00343
ACS Chem. Neurosci. 2016, 7, 599–614

compared with model 2 with recovery of 13% and model 3 with a slight recovery of 2%. In addition, it is turn content transformed into helix in CQ_1−1 and −2, and β-sheet content transformed into helix in CQ_1−3. Therefore, Cu^{2+} chelation can induce the S1 → S2 transition of $A\beta_{40}$, whereas the addition of CQ_1 can reverse the transition, demonstrating strong potential of CQ_1 in disaggregating Cu^{2+}−$A\beta_{40}$ complexes and reducing neurotoxicity.[62,66]

3.2.2.1.2. Efficacy of CQ_2 and CQ_3. Different from CQ_1 in structure, both CQ_2 and CQ_3 have a polar group of R = Cl and NO_2 and produce different recovery effects on the models *x* aggregates. Result showed that CQ_2 can recover the helix content of the three models *x* in the following rank: CQ_2−1 (+25%) > CQ_2−2 (+9%) > CQ_2−3 (+5%), indicating that CQ_2 also produces the strongest recovery effect on model 1, as CQ_1 does. Therefore, both CQ_2 and CQ_1 may recover more helix in the low-pH model 1 than in the high-pH models 2 and 3.The increasing helix content from the addition of CQ_3 in the three models *x* can be ranked as CQ_3−1 (18%) > CQ_3−3 (10%) > CQ_3−2 (9%), indicating that CQ_3 has the best effect on model 1 at low pH.

3.2.2.2. Helix of the Identical Model x Recovered by Different Drugs CQ_i. The helix contents in the three systems are 67% (CQ_1−1), 66% (CQ_2−1), and 59% (CQ_3−1), higher than that in $A\beta_{40}$ monomer (53%) and model 1 (41%), indicating that the existence of CQ_i not only inhibits the transition from S2 to S3 in model 1 at low pH but also promotes the backward transition (from S2 to S1). This is also in accord with experimental results that the addition of CQ_i can inhibit the aggregation of Cu^{2+}−$A\beta_{40}$ at pH = 6.6.[24] In comparison with the four regions in the full-length $A\beta_{40}$, the NT region contributes most to the transitions, indicating that the four residues in the Cu^{2+}-coordination sphere play key roles. As two core residues for Cu^{2+} coordination in the sphere,[13] Asp1 and Ala2 have little helix content and stay consistent before or after Cu^{2+} or CQ_i addition (Figures 3 and S5). His6 has 65% helix content in the $A\beta_{40}$ monomer. The content degenerates to ca. 21% in model 1 but recovers to 100% upon addition of any of the three CQ_i. His13 in $A\beta_{40}$ monomer has ca. 45% helix content, whereas Cu^{2+} coordination in model 1 can increase it to 100% and addition of any of the three CQ_i hardly affects the contents. Therefore, only two histidine residues in the low-pH coordination sphere of {O^{A2}, N^{D1}, N^{H6}, N^{H13}} vary intensely but differently. In addition, CQ_i make the CHC and CT regions in model 1 full of helix content, indicating excellent recovery effect for the two regions, from which β-sheets are generated.

The recovery of helix in model 2 is 13% (CQ_1−2), 9% (CQ_2−2), and 9% (CQ_3−2) after the three CQ_i are added, revealing that CQ_1 with R = H has the strongest effect on the recovery of model 2 at high pH (8−9). As two components of Cu^{2+} coordination, Ala2 and His6 always preserve some helix content whether or the CQ_i are present, indicating that CQ_i cannot recover these two residues (Figures 3 and S5). It is interesting that the helix content of other components, His13 and His14, in model 2 do not rise but fall instead after CQ_i addition, indicating that the helix recovery mainly comes from the contribution of the $A\beta_{17-40}$ (Figure S5). For another high-pH structure, model 3, the recovery of helix content is 10% (CQ_3−3), 5% (CQ_2−3), and 2% (CQ_1−3) after the corresponding CQ_i interacts with model 3. Meanwhile the β-sheet content (2%) in the initial model 3 disappears and the secondary structure of model 2 transforms from S3 → S2 → S1. Except for two main differences, most helix propensity in the metal coordination sphere is similar to model 2. The two differences are that (1) CQ_2 is the only drug that can recover helix content of His13/His14 of model 3 completely, but with less recovery for CT regions compared with either CQ_1 or CQ_3 and (2) helix recovery of both CHC and CT regions in CQ_3−3 are the highest among the three CQ_i−3 counterparts, whereas the recovery in three CQ_i−2 are almost equal (Figure S5). These results manifest that all the three CQ_i have recovery effects on $A\beta_{40}$ in model 3, and the recovery effects of CQ_3 (R = NO_2) are stronger than those of CQ_1 (R = H) and CQ_2 (R = Cl). Similar transition and recovery effects were also observed in the inhibition study for the EGCG−$A\beta_{42}$ aggregation system.[61] In short, CQ_1 can have the strongest effect on model 2, whereas both CQ_2 and CQ_3 have strongest effect on model 1. For model 3, CQ_3 is the optimal inhibitor.

3.3. Binding Energy between CQ_i and Model *x*: MM-PBSA Analysis. Binding free energies between CQ_i and the three models were shown in Table 2. It can be observed that these energies vary widely from −44.9 to −125.3 kJ/mol, indicating different binding modes and concomitant different numbers of contacts. In detail, the binding energies between three CQ_i and model 1 at low pH are −65.6, −125.3, and −97.7 kJ/mol, respectively, indicating that the interaction between CQ_2 and model 1 is the strongest and atomic contact number the highest (Figure 4). The binding energy between CQ_i and high-pH model 2 can be ranked as −109.4 (CQ_1−2) > −89.3 (CQ_2−2) > −83.4 kJ/mol (CQ_3−2), roughly matching with the rank of the atomic contact numbers between CQ_i and model 2. The reasonable consistency between binding energy and the corresponding contact number indicates that the binding strength between CQ_i and Cu^{2+}−$A\beta_{40}$ can be assessed mainly by their contact number, in combination with interaction modes and spatial relationships. Likewise, the ordering of binding energy between CQ_i and model 3 is −80.7 (CQ_3−3) > −51.5 (CQ_2−3) > −44.9 kJ/mol (CQ_1−3). A comparison for energy terms (ΔE_{elec}, ΔG_{GB}, and ΔG_{np}) revealed that the ΔE_{vdw} makes a dominant contribution to the entire binding energy in all these complexes, as observed by Ngo et al.[67] Although the ΔE_{elec} contribution in CQ_2−3 (−35.6 kJ/mol) is far greater than that in CQ_3−3 (−9.5 kJ/mol) and indicates that the binding energy of CQ_2−3 should also be larger potentially than the CQ_3−3, it is actually not the case due to the offset effect from more positive ΔG_{GB} (88.6 kJ/mol) of the former. Generally, the stronger binding energy between drugs and Aβ aggregate is, the more powerful the inhibition and disaggregation ability of a drug and the less neurotoxicity would

Table 2. Binding Free Energy and the Corresponding Contributions (kJ/mol) between CQ_i and Model *x* Obtained by the MM-PBSA Method

	ΔE_{vdw}	ΔE_{elec}	ΔG_{GB}	ΔG_{np}	ΔE_{bind}
CQ_1−1	−92.4	−4.9	42.2	−10.5	−65.6
CQ_1−2	−164.7	−18.7	89.1	−15.1	−109.4
CQ_1−3	−58.2	−10.1	32.0	−8.6	−44.9
CQ_2−1	−177.4	−17.6	85.0	−15.3	−125.3
CQ_2−2	−129.5	−55.5	109.8	−14.1	−89.3
CQ_2−3	−93.3	−35.6	88.3	−10.9	−51.5
CQ_3−1	−127.8	−9.8	53.5	−13.6	−97.7
CQ_3−2	−118.6	−60.0	108.9	−13.7	−83.4
CQ_3−3	−97.5	−9.5	37.9	−11.6	−80.7

DOI: 10.1021/acschemneuro.5b00343
ACS Chem. Neurosci. 2016, 7, 599−614

Table 3. Binding Energies (in kJ/mol) between CQ_i and Four Regions of Model *x*

	CQ_1−1	CQ_1−2	CQ_1−3	CQ_2−1	CQ_2−2	CQ_2−3	CQ_3−1	CQ_3−2	CQ_3−3
NT	−0.58	−16.33	−0.19	−15.77	−7.35	−8.76	−7.78	−8.11	−9.85
CHC	−6.00	−11.42	−2.95	−11.08	−5.67	−6.58	−8.49	−3.34	−6.91
FL	−1.80	−6.04	−4.50	−6.94	−14.41	−0.38	−2.33	−8.93	−8.03
CT	−20.90	−14.26	−15.81	−28.10	−13.45	−2.71	−29.48	−21.35	−18.87

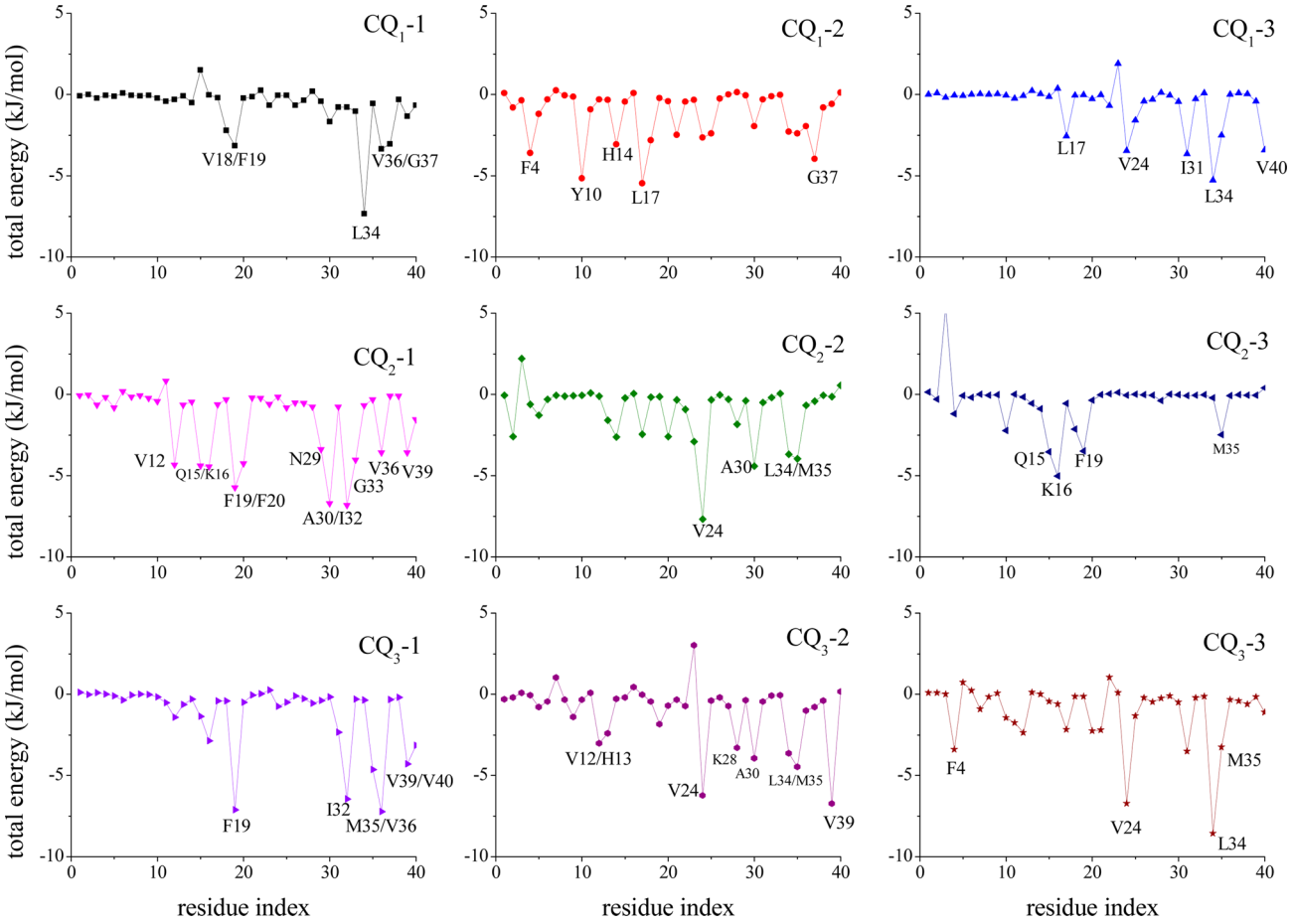

Figure 5. Binding energies between CQ_i and residues of model *x*. Single-letter abbreviations for residues were used to save the space.

be.[66] Because $CQ_{2,3}$ drugs with the polar groups (R = Cl, NO_2) can bind model 1strongly (−125.3 and −97.5 kJ/mol), they should both have good performance in disaggregating model 1. Moreover, the two binding energies are far larger than that of CQ_1 with R = H, indicating the disaggregation ability of CQ_2 > CQ_3 > CQ_1. The result is well consistent with the experimental result of Geng et al.[24] that both CQ_2 and CQ_3 produce a stronger disaggregation effect on $A\beta_{40}$ aggregates than CQ_1 at low pH (pH = 6.6), where the binding strength was measured to be in the order CQ_3 > CQ_2 > CQ_1. The difference in binding ordering for CQ_2 and CQ_3 may derive from two aspects. (1) The experimental result[24] was measured from the $A\beta_{40}$ aggregate, whereas the present is from $A\beta_{40}$ monomer in which the intermolecular interactions of $A\beta_{40}$ are absent. (2) Given the coexistence of two main species, **I** and **II**, in the physiological pH range,[68,69] the contribution of the binding energy from **II** should also be included although it is minor at the low pH state.[68−71] In the present study, only two most stable **IIa** subspecies were taken into account for computational simplicity. Based on the more stable IIa_$\varepsilon\delta\varepsilon$ (than IIa_$\varepsilon\varepsilon\varepsilon$),[13] model 3 should also contribute more than model 2 to the entire binding energy in the physiological pH condition. The binding between CQ_i and model 3 was predicted in the following ordering, CQ_3−3 > CQ_2−3 > CQ_1−3, coinciding exactly with that of the Geng et al's experiment.[24] As a criterion for a drug screening, not only the strong binding ability but also the aqueous solubility, lipophilicity, and BBB permeability[24,26] etc. should be taken into account. In the light of the binding strength rank, CQ_2 and CQ_3 are better candidates than CQ_1 to disaggregate the Aβ at lower pH (model 1). For the aggregates obtained at high pH, CQ_1 is the most powerful and both CQ_2 and CQ_3 are also competitive for model 2. CQ_3 is the best candidate for disaggregating model 3 (CQ_3−3, −80.7 kJ/mol). The conclusion is exactly agreement with that obtained from the contact number analyses above.

3.4. Sites and Mechanisms of Binding between CQ_i and Model *x*. To determine the primary sites and mechanism of binding between CQ_i and model *x*, the contributions of binding energy from four regions (see definitions for regions in Figure 1) of $A\beta_{40}$ monomer are shown in Table 3. The animations displaying the dynamic processes of CQ_i−model *x* interaction are shown in Movies S1−S9 in SI. Only the regions

DOI: 10.1021/acschemneuro.5b00343
ACS Chem. Neurosci. 2016, 7, 599−614

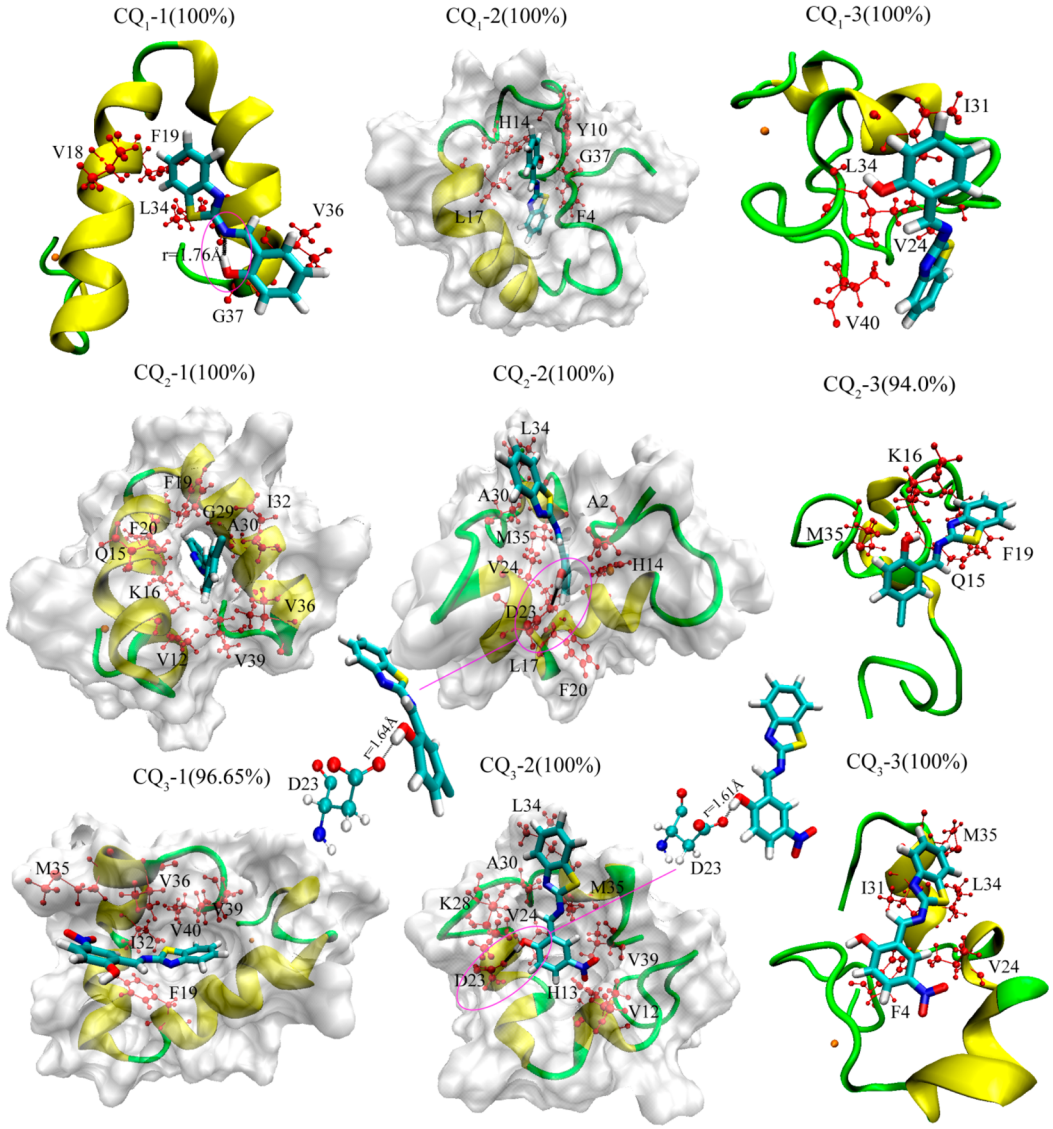

Figure 6. Morphologies of CQ_i−*x* obtained by g_cluster with cutoff = 0.15. The data in parentheses are the populations. Drug molecule CQ_i is shown in licorice and the contact residues of model *x* in ball−stick (red). The black line in CQ_1−1 (circled in pink) shows the intramolecular H-bonding between N14 and H27 (-O26) in CQ_1. The black lines in CQ_2−2 and CQ_3−2 show the H-bonding between Asp23 and CQ_i.

with binding energy over 10 kJ/mol were taken as the main interaction regions and discussed in the following sections.The binding energy contributions of every residue in each region are shown in Figure 5.

3.4.1. CQ_1−x. In CQ_1−1, the main interaction region is CT (−20.9 kJ/mol), whereas the NT (−0.6 kJ/mol), CHC (−6.0 kJ/mol), and FL (−1.8 kJ/mol) regions have minor contributions to the entire binding energy, indicating that those residues in the NT region are hardly affected by drug CQ_1. In other words, CQ_1 does not chelate directly with Cu^{2+} or related residues. In the CT region, Leu34 and Val36 and Gly37 residues play key roles and account for 66.5% contributions to it. A previous study had determined that the mutation of L34C can destroy the formation of Aβ hexamer and tetramer.[72] Moreover, Ile32 and Leu34 located at the Aβ protofibril center can maintain the stability of the Asp23−Lys28 salt bridge and prevent the hydrophilic charged groups from exposing to the solvent excessively. Mutation of I32G or L34G can break the Asp23−Lys28 salt bridge and quickly dissolve it, which destroys the stability of the protofibril.[73] Therefore, the binding of CQ_1 to the CT region is beneficial not only to dissolve the fibril and reduce the toxicity but also to inhibit the transformation from S2 to S3 (β-sheet). Phe19 and Val18 in the CHC region account for 88.3% binding energy and also play key biological roles. For example, Phe19/Leu34 contact is the key to maintain 2-fold Aβ_{40} fibrils internal quaternary.[74] The strong interaction between Phe19/Leu34 and CQ_1 can prevent Aβ_{40} monomer from forming fibrous structure further. The CQ_1−1 structure (Figure 6) clearly shows that Aβ_{40} displays a U-shape with two long helix sequences of Tyr10−Glu22 and Gly25−Gly37, where the CQ_1 molecule locates over and between the two helices. The dynamic process of CQ_1−model 1 interaction can be observed clearly from movie S1, in which phenol and benzothiazole rings of CQ_1 are rotating around the C7−N14 bond with the average angle (see red lines in Figure 4) of about 28.9°. The relatively small fluctuation around 28.9° derives from generation of the intramolecular H-bond O26−H27···N14 (1.76 Å) of CQ_1, which limits the rotation of the two rings and results in the benzothiazole ring locating on Val18, Phe19, and Leu34 and the phenol ring on

DOI: 10.1021/acschemneuro.5b00343
ACS Chem. Neurosci. 2016, 7, 599−614

Val36 and Gly37 hydrophobic residues, indicating that the hydrophobic effect plays an important role in the binding process.

Different from CQ_1−1, the main contributing residues in the NT region of CQ_1−2, not only include Phe4, and Tyr10 but also His14, a key site for Cu^{2+}coordination.[13]Therefore, the strong interaction between His14 and CQ_1 would be beneficial to slow amyloid aggregation induced by Cu^{2+}. .Figure 6 shows that drug CQ_1 inserts in the U-shaped Aβ_{40} chamber that contains a long helix sequence (Leu17−Lys28), where the phenol ring of CQ_1 mainly contacts the cavity formed by hydrophobic residues Tyr10, His14, and Leu17 and the benzothiazole ring mainly contacts the side chains of Phe4, Val24, Ala30, Leu34, and Met35 (movie 2). It is noted that CQ_1 affects the Cu^{2+} coordination sphere and morphology of model 2 through impacting on the surrounding residue His14, rather than through direct chelating with Cu^{2+} although CQ_1 is close to Cu^{2+} in space. Binding energy data reveal that the interaction between CQ_1 and model 2 is also the strongest. Similar to the case in CQ_1−1, CT (−15.8 kJ/mol) is the main region for CQ_1 to binding CQ_1−3. The cluster structure (100%) shows that Aβ_{40} in CQ_1−3 features a random coil morphology, where CQ_1 attaches on the Aβ_{40} surface with the benzothiazole ring locating at the side chains of Val24, Leu34, and Val40 residues and the phenol ring at Ile31 residue. The dihedral angle between the phenol ring and the benzothiazole ring fluctuates averaging about 148.2°, being significantly larger than that in either CQ_1−1 or CQ_1−2. Movie S3 animates the process of CQ_1 over the Aβ_{40} surface, indicating lower contact number and resultant weaker binding strength.

3.4.2. CQ_2−x. In CQ_2−1, the highest binding energy contribution is also from CT (−28.1 kJ/mol) region and the two minor ones are NT (−15.8 kJ/mol) and CHC (−11.1 kJ/mol) regions. There are five residues, Ala30, Ile32, Gly33, Val36, and Val39, in CT to directly react with CQ_2. Among these residues, structures of Gly33 and Gly38 change greatly with wide helix content recovery after drug CQ_2 is bound (comparing Figure 3 with FigureS5). The cluster structure (100%) of CQ_2−1 shows that CQ_2 drug inserts obliquely in the U-shape Aβ_{40} cavity, which is responsible for the largest binding strength. Figure 5 (see CQ_2−1) clearly displays that almost entire CQ_2 molecule is surrounded by the hydrophobic loop formed by ambient residues, with the rotation angle between two rings constantly changing at about 36.0° during CQ_2 approach to and insertion into model 1 to generate a relaxed CQ_2−1 complex (movie S4). The Aβ_{40} morphology in CQ_2−2 features a large amount of coil content during interaction with CQ_2. It is noted that there is a stable H-bond O−H···O (1.64 Å) generated between the phenolic hydroxyl group of CQ_2 and carboxylate oxygen of Asp23, causing Asp23 and its adjacent residue Val24 have strong binding to CQ_2. Salt bridge Asp23−Lys28 plays an important role in maintaining protofibril stability,[73] so the H-bond would greatly destroy the stability of the protofibril. In the reaction process, the rotation angle changes widely from 50° to 180°, indicating that the two rings of CQ_2 have to constantly adjust their orientation to match their ambient residues (movie S5) until equilibrium. The angle fluctuation remains at about 157.5° in the relaxed state (Figure 4), which just approaches the local minimum on its PES (Figure 7C), indicating a stable state on the premise of making it the best match to Aβ_{40}.

In CQ_2−3, the residues Gln15 and Lys16 (NT) and Phe19 (CHC) are major contributors to binding energy. Obviously,

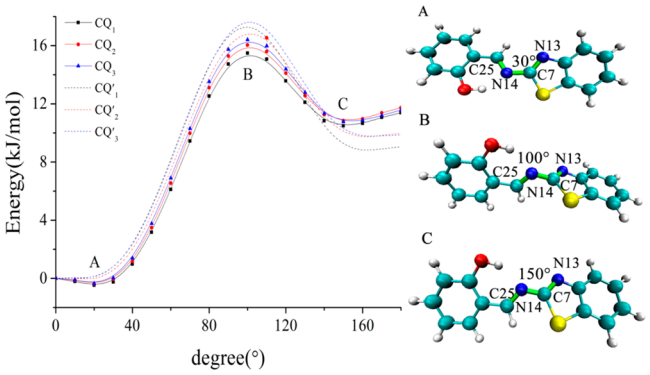

Figure 7. Potential energy surfaces (PESs) of CQ_i along with the rotations of dihedral angles ($\angle C_{25}N_{14}C_7N_{13}$) using both M062X/6-31+G* (in solid line) and B3LYP/6-31G* (in dashed line and marked in CQ_i') methods in combination with the z-matrix optimization. A, B, and C points denote global minimum, transition state, and the local minimum on the PES, corresponding to dihedral angles 30°, 100°, and 150°, respectively. Only the geometries of CQ_1 obtained by M062X/6-31+G(d) method, taken as examples of CQ_i, at the three points were illustrated on the right.

these bindings will play an important role in Aβ protein disaggregation. For example, experiments had determined that the K16A mutation could impact Aβ self-assembly and reduce remarkably the toxicity of A$\beta_{40/42}$ peptides,[75] whereas familial Aβ K16N peptide[76] itself is not harmful to neuronal cells but becomes toxic once it is mixed with Aβ. Other studies also suggested that Lys16 is apt to expose to solvent and interact with other monomers during Aβ aggregating.[77,78] Thus, Lys16 can play a positive role in disaggregating the Aβ and reducing the toxicity of Aβ aggregates by binding CQ_2 strongly. Aβ_{40} morphology in CQ_2−3 characterizes a random coil structure with CQ_2 interacting on the Aβ_{40} surface. As a result, a relative weaker binding energy of −51.5 kJ/mol is obtained. On the Aβ_{40} surface, the two rings in CQ_2−3 still need to rotate flexibly in the range of 0−180° to maximize their match to the corresponding residues. Finally, the benzothiazole ring of CQ_2 was observed to be close to residues Gln15 and Lys16 of NT and Phe19 of CHC, and the phenol ring to residue Met35 of CT (movie S6).

In comparison with CQ_1, CQ_2 has a polar group of R = Cl that affects greatly the regions of model *x* to bind with it. In the three CQ_2−*x* complexes, the main binding regions not only include CT but also the NT, indicating that the main binding residues include not only the hydrophobic ones but also charged ones (His13/His14). These charged residues were confirmed to be associated closely with the toxicity of Aβ,[79] whereas the binding contributions from the NT region in CQ_1−1 and CQ_1−3 complexes are almost negligible, indicating that CQ_2has a better treatment potential than CQ_1 for AD originating from aggregation in the NT region.

3.4.3. CQ_3−x. In CQ_3−1, the CT (−29.5 kJ/mol) is the core region for CQ_3 binding. The corresponding binding strength is more than three times as much as NT (−7.8 kJ/mol) or CHC (−8.5 kJ/mol). The main residues participating in the CT region are Ile32, Leu34, Met35, Val39, and Val40, and in CHC the main participating residue is Phe19. Given that Phe19 is a key residue to build Aβ fiber quaternary structure,[74] the stronger binding between Phe19 and CQ_3 will greatly damage the stability of fibril or reduce the probability of fibril formation. Cluster structure (96.7%) shows that CQ_3 obliquely inserts into

DOI: 10.1021/acschemneuro.5b00343
ACS Chem. Neurosci. 2016, 7, 599−614

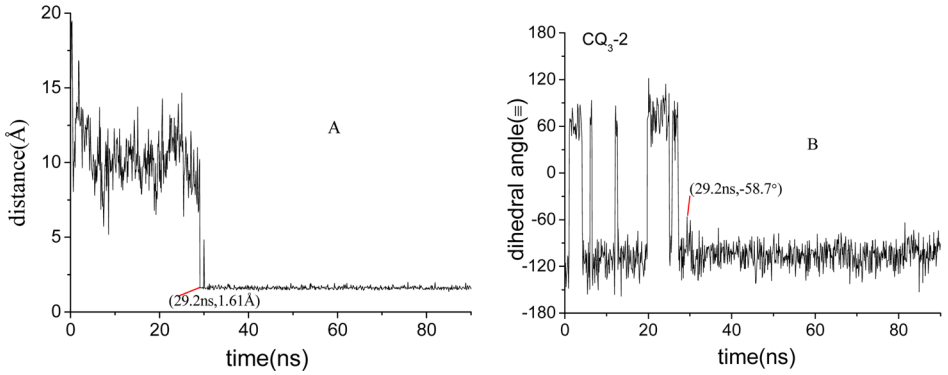

Figure 8. H-bonding between Asp23 and CQ_3 in CQ_3−2. (A) Time evolution of the distance between H atom of OH in CQ_3 and O_{D1} in Asp23. (B) Time evolution of the dihedral angle $\angle O_{D1}C_GC_BC\alpha$ in Asp23 in CQ_3−2. The red lines marked the parameters at critical points of H-bond formation.

the two helix sequences of Tyr10−Phe20 and Asp23−Val36 and generates higher contact number and stronger binding (−97.7 kJ/mol).With the benzothiazole ring inserted between the two helix sequences, the phenol ring of CQ_3 approaches residues Phe19, Ile32, Met35, and Val36 and generates strong residue−drug interaction. Once equilibrium state is achieved (>40 ns), the rotation angle fluctuates around 143.8° (see movie S7), corresponding to the local minimum of CQ_3 on its PES (Figure 7C).

The main interaction region in CQ_3−2 is also CT (−21.4 kJ/mol) with NT (−8.1 kJ/mol) and FL (−8.9 kJ/mol) as minor regions. Cluster result shows that CQ_3 partly inserts into the disordered structure with the benzothiazole ring close to Ala30 and Leu34 and the phenol ring close to Val12, His13, Val24, Met35, and Val39 residues. Noted that there is a stable H-bond, O−H···O (1.61 Å), generated between the phenolic hydroxyl groups of CQ_3 and carboxylate oxygen of Asp23, heralding a potential strong interaction between them. In fact, the calculated binding energy contribution of Asp23 is a positive value (3.0 kJ/mol), opposite to initial expectation. Figure 8 disclosed that the dihedral angle of $O_{D1}-C_G-C_B-C_\alpha$ in Asp23 swings occasionally between 60° and −120° until the H-bond generates. The angle fixes at about −120° and corresponds to a stable H-bond with 1.61 Å distance after MD time exceeds 29.2 ns. Time evolution vs the H-bond distances in Figure 8A confirms that the H-bond is not only stable but also persistent. Therefore, the adverse binding contribution from Asp23 can be attributed to serious deformation induced by the H-bonding. As a key residue in salt bridge Asp23−Lys28,[73] Asp23 can hardly link Lys28 if it deforms. As a result, a hairpin structure will be not produced for a $A\beta_{40}$ monomer or the stability of an established $A\beta_{40}$ protofibril will be destroyed. On this scale, CQ_3 is a significant candidate drug for disaggregation or inhibition of the $A\beta_{40}$ aggregate (in model 3) although its binding energy (−83.4 kJ/mol) is smallest among its counterparts of CQ_1 (−109.2 kJ/mol) and CQ_2 (−89.3 kJ/mol). The result also accounts well for why the CQ_3 has the best disaggregation activity among the three CQ_i drugs.[24] Without the H-bond between Asp23 and CQ_3, CQ_3 might locate on the surface of $A\beta_{40}$ instead of inserting partly into it. The rotation between the two rings is from 50° to 180° with less fluctuation around 159.6° after the system reaches equilibrium (>60 ns) (movie S8). As it does in CQ_3−2, CQ_3 in CQ_3−3 also mainly binds to the CT (−18.9 kJ/mol) region with binding strength as much as twice of that of NT (−9.9 kJ/mol) or FL (−8.0 kJ/mol) regions but without the H-bond generation. Meanwhile $A\beta_{40}$ in CQ_3−3 displays a random coil structure with CQ_3 locating on its surface, whereas the rotation angle of CQ_3 also keeps fluctuatiing around 152.5° after equilibrium (>350 ns).

3.5. Assessment of CQ_i. *3.5.1. Structural Characteristics of CQ_i Drugs.* Because the rotation angle between the phenol ring and benzothiazole ring of CQ_i changes constantly during the interaction between CQ_i and model *x*, we calculated the PES along with the angle change and found that the change tendencies of either PES or rotation angle are consistent with each other for the three drugs (see Figure 7). Likewise, M062X results are in good agreement with the B3LYP ones but with more specific minima on the PESs. Therefore, the following discussions are based on these M062X results. When the rotation angle is in the range of 0−30° (approximate a planar structure), the potential energy of the CQ_i is the lowest (ca. 25°). With the increasing rotation angle, the potential energy increases gradually. When the rotation angle reaches 100°, the energies grow up to 15.5, 16.0, and 16.4 kJ/mol for CQ_1, CQ_2, and CQ_3, respectively, relative to each ground-state planar counterpart. After passing the energy peaks, the energies drop rapidly until the angles reach 150−180°, where the downtrends slow and approach a plateau, indicating a local minimum (ca. 150°) of CQ_i. The local minimum is 9−10 kJ/mol over the ground-state CQ_i. MD results revealed that the larger rotation barriers (15.5−16.4 kJ/mol) in the three CQ_i do not prevent their rotation around the C7−N14 bond so that the maxima match with $A\beta_{40}$ peptide and the greatest atomic contact number can be achieved. It is obvious that the rotation between the two rings provides great convenience for CQ_i drugs to insert flexibly into the hydrophobic cavity of $A\beta_{40}$. The result also sets a new direction toward the drug design in treatment of AD, that is, the drugs with two aromatic rings linked by a rotation bond will be favorable to the interaction between the drug and corresponding peptide aggregate. In addition, observations from Figure 4 revealed that the rotation angle of CQ_1 fluctuates around 20−30° in both relaxed CQ_1−1 and CQ_1−2 structures, corresponding to the most stable state of CQ_1 (Figure 7A). The angles of CQ_i in CQ_1−3, CQ_2−2, CQ_3−1, CQ_3−2, and CQ_3−3, however, move to about 150°, an angle preserved by the local minimum states on the corresponding CQ_i PESs (Figure 7C). Obviously, the higher energy (10.5−10.8 kJ/mol) of the C-state structure than the counterpart of A-state would be responsible for the decreased binding strength of these C-state complexes. Interestingly, the angle of CQ_2 in CQ_2−3 just fluctuates around 100°, corresponding to the

DOI: 10.1021/acschemneuro.5b00343
ACS Chem. Neurosci. 2016, 7, 599−614

transition state (B) between A-state and C-state. Moreover, the fluctuation amplitude around 100° is the highest among all these CQ_i−x complexes, accounting for partly why CQ_2−3 has the weakest binding strength among the three CQ_2−x complexes. That is, not only the model 3 itself (i.e., deformation of Asp23 induced by H-bonding between CQ_3 and Asp23, see Figure 8) in CQ_2−3 contributes to the lower binding energy, but also the high-energy state (B) CQ_2 itself (~16.4 kJ/mol more than A-state) goes against the binding between CQ_2 and model 3.

3.5.2. The Results from Docking Are Different from Those of MD. Docking results showed that these CQ_i molecules only attach on the surface of Cu^{2+}−Aβ_{40} with weaker binding energies in the range of −4.2 to −5.7 kJ/mol (see Table S7). In the relaxed complexes (after MD simulations), the binding energy values increase from −44.9 to −125.3 kJ/mol because CQ_i inserts into the hydrophobic cavity of Aβ_{40} partly or fully and forms stronger binding. The result strongly suggests that MD simulated results instead of docked ones can reflect the reality of drug−ligand reaction. In addition, the drug with weak binding strength always locates on the surface of Aβ_{40}, indicative that in such weak-binding case, the binding strength or site from docking should be closer to the counterpart from MD simulation.[16]

3.5.3. Relationship between Binding Strength and Binding Location. The strong binding energy indicates that CQ_i insert into the inner of Cu^{2+}−Aβ_{40} complex and form more contact with surrounding Aβ_{40} residues. On the contrary, the weak binding energy implies that CQ_i attaches at the surface or at best partly inserts into the hydrophobic cavity of Aβ_{40} and partly exposes to the solvent. For example, CQ_1 and CQ_2 fully insert in model 2 and model 3, respectively, with binding energy more than 100 kJ/mol in CQ_1−2 and CQ_2−1. CQ_1 and CQ_2 mainly locate on the surfaces of Aβ_{40} with weak binding strengths of −44.9 and −51.5 kJ/mol, respectively, in CQ_1−3 and CQ_2−3. Likewise, inhibitors derived from peptides and their derivatives often attach on the surface of Aβ with hydrophobic interactions or H-bonding interactions and consequently produce weak binding strength. For example, the interaction strengths between Aβ and its fragment KLVFF or fragment derivative LPFFD are only −29.7 and −54.8 kJ/mol, respectively.[16] The lower binding strength of KLVFF than its derivative was attributed to the latter having higher hydrophobicity, indicating that the lower the hydrophobicity is, the better the inhibitory capacity will be.[16] The present result also confirms this point that $CQ_{3/2}$ have stronger disaggregation effect than CQ_1 on Aβ aggregate (model 1 and model 3) induced by Cu^{2+}. CQ_1 has higher hydrophobicity and also greater disaggregation effect than CQ_2 and CQ_3 on the Aβ aggregate (model 2) induced by Cu^{2+}, however, clashing with above-mentioned viewpoint. Thus, the relationship between hydrophobicity of a drug and the corresponding inhibitory capacity remains open and depends on the types of aggregation and environment.

3.5.4. Natural Polyphenol Drugs. The EGCG molecule[17,18,61] contains three aromatic rings, which are easier to rotate around the C−C bonds linking two of three rings. Because of three rings orienting each to three separate directions in space, the entire EGCG molecule is difficult to insert into Aβ_{1-42} to form more interatomic contacts. Liu et al.[61] found that the interaction between ten EGCG molecules and an Aβ_{1-42} monomer depends on the hydrophobic effect and π−π stacking, determining that the binding energy between the Aβ_{1-42} monomer and each EGCG molecule is only −25.9 kJ/mol on average. Such a low binding strength indicates that each EGCG molecule only attaches on the surface of the Aβ_{1-42} monomer rather than inserting into it. Curcumin has two aromatic ring groups connected by a rotated flexible C−C bond, indicating a favorable interatomic contact between the curcumin and the Aβ. Ngo et al.'s result[67] verified that curcumin can attach on the surface of Aβ_{40} and even partly insert into Aβ_{40} aggregate, causing relatively high binding strength (−80.3 kJ/mol) and resultant powerful ability for inhibition and disaggregation.[67] In contrast, either ibuprofen or naproxen has only one aromatic ring and attaches on the Aβ_{40} surface; thus the interaction between ibuprofen or naproxen and Aβ_{40} is weak (−36.4 or −13.3 kJ/mol).[67] The weak binding energy is derived from the interaction between the only ring of the drug and both CHC and CT regions of Aβ_{40} with hydrophobic effect and H-bond interaction.[67]

As a synthetic compound, NQTrp[19,20] contains a naphthalene ring and a quinoline ring connected by their C−C bond. Zhang et al.'s result showed that NQTrp is coated by the binding pocket formed by residues of Aβ_{1-42} dimer. According to the residue contribution data in Zhang's report,[20] we speculated that the binding energy between two NQTrp and the Aβ_{1-42} dimer is about over −200 kJ/mol. Then the average of binding energy between a single NQTrp and Aβ_{1-42} monomer should also be more than −100 kJ/mol, further confirming that an insertion mechanism for a drug is favorable to the binding. The key binding sites in the "pocket" are hydrophobic residues Phe19 and Phe20 in CHC and Leu34 and Met35 in CT and hydrophilic residues Arg5, Asp7, Tyr10, His13, and Lys16 in NT.

3.5.5. Analysis and Prospective. Both KLVFF and LPFFD and EGCG molecules are apt to attach on the surface rather than insert into the interior of Aβ. As a result, the interaction energy is low, indicating a poor disaggregation effect. Both NQTrp and the present CQ_i are composed of two aromatic rings connected by a C−C(N) bond, which can flexibly rotate to favor insertion into the Aβ monomer or dimer and achieve maximum match with the ambient residues of the Aβ. Hence large binding energy (usually over −80 kJ/mol) and strong disaggregation effect can be observed. Especially for the Aβ system bound by a Cu^{2+}, CQ_3 with a strong polar group is better than CQ_1 with strong hydrophobicity in decreasing Aβ aggregation and reducing toxicity, which is consistent with experimental results.[24] By extension, if a drug molecule contains two aromatic rings linked by a flexible rotation bond, then such a structural feature would be greatly favorable to increase its contact with the ambient Aβ aggregate(s) by inserting itself into the interior of the Aβ molecule(s). As a result, the increased contact number can greatly disaggregate the Aβ aggregate and attenuate the toxicity of the Aβ aggregate. Referring to the effect of EGCG inhibitor reported by Liu et al.,[61] we suggested that the aromatic group of a drug should not be too bulky, and the links between two aromatic groups in a drug molecule with more aromatic groups should be "in series" instead of "in parallel" so that the drug can insert into a Aβ aggregate to generate the most contacts. The bonds linking two aromatic groups in a drug in "in parallel" or "radial" mode would restrain it to insert into Aβ monomer or among Aβ aggregates and decrease its inhibition effect.[17,18,61] For the drug molecules with aromatic rings linked in "in series" mode, appropriate modification with polar group(s) on some group is more effective to inhibit the aggregation of those peptides with

DOI: 10.1021/acschemneuro.5b00343
ACS Chem. Neurosci. 2016, 7, 599−614

strong hydrophilic group and electrophilic group.[24] For example, the presence of NO_2 group reduces the hydrophobicity of CQ_3 and enables CQ_3 to form strong contact not only with CT and CHC but also with Val12 and His13 of the NT region of Aβ_{40} in CQ_3−2. CT and CHC regions are known as key regions to form β1-sheet and β2-sheet in fiber,[54] and His13 in the NT region is a key residue to bind to Cu^{2+};[9,13]hence stronger binding from CQ_3 will have great inhibition effect on Aβ_{40} aggregates and disrupt the stability of the Aβ_{40} fibril.

4. CONCLUSIONS

In this article, we studied the disaggregation mechanisms of Cu^{2+}−Aβ_{40} complexes formed in different pH solutions when three small drug molecules CQ_i are present. The presence of CQ_i not only inhibits the aggregation of Aβ_{40} induced by Cu^{2+} binding but also recovers largely the secondary structure character of the original Aβ_{40}. In detail, Cu^{2+}binding alters the composition of secondary structures of Aβ_{40} monomer by decreasing the population of helix and increasing the turn and coil populations in the process of aggregation evolution of helix (S1) → coil/turn (S2) → β-sheet (S3).[54] The population transitions of S1 → S2 in model 2 and model 3 are more obvious, indicative that the high-pH Cu^{2+}−Aβ_{40} products are more apt to aggregate. However, the interaction between CQ_i and model *x* not only inhibits the S1 → S2 transition but also promotes the reverse transition of S2 → S1.

As a Cu^{2+}−Aβ_{40} complex generated at low pH,[9−12] model 1 can bind either CQ_2 or CQ_3 more strongly than CQ_1 because the former two drugs with polar groups can bind strongly to the residues located at not only hydrophobic CT regions but also the hydrophilic and charged NT regions of Aβ_{40}, whereas CQ_1 can only bind to those in the CT region. The result is consistent with the experimental determination obtained at pH = 6.6.[24] Thus, for Aβ_{40} aggregates induced by a Cu^{2+} at lower pH, drugs with polar group(s) are more effective inhibitors. If the aggregates are produced at higher pH and in modes of IIa_$\varepsilon\delta\varepsilon$ and IIa_$\varepsilon\varepsilon\varepsilon$[13] (corresponding to models 2 and 3), then the choice for inhibitor would be different. For model 2, the binding of CQ_1 over CQ_2 or CQ_3 is more favorable to inhibit the Aβ_{40} aggregation. The stronger H-bond between Asp23 and CQ_3 not only can prevent the potential formation of salt bridge Asp23−Lys28[73] in Aβ_{40} monomer or oligomer but also can destroy the stability of a formed fibril. Therefore, CQ_3 is the best potential drug candidate from the H-bond point of view. For model 3, CQ_3 has stronger ability for disaggregation than either CQ_2 or CQ_1. The different efficacies of three drugs on model 3 indicate that the selection of a drug not only depends on the polarity of the molecule but also takes into account the acidic environment of Cu^{2+}−Aβ_{40} formation. Taken together the coexistence of two main species **I** and **II** in the physiological pH range[68,69] and thus unneglected contribution of **II** species to the binding energy at low pH[68−71] as well as the above analysis accounts well for why CQ_3 has greater inhibition/disaggregation effects than CQ_2 on model 1 experimentally at pH = 6.6.[24]

MM-PBSA results revealed that the major contribution for the interaction between CQ_i and Cu^{2+}−Aβ_{40} is van der Waals' force, and CQ_2 has the largest binding energy in model 1. Unlike the chelation between salicylaldehyde of the Schiff base in CQ and Cu^{2+} of model *x*,[20] CQ_i can bind model *x* by inserting its two rings into the hydrophobic cavity of Aβ_{40} peptide through hydrophobic effect, partial π−π stacking interaction, H-bond effect, etc., presenting an "insertion mechanism".[22] The main residues involved in the cavity include Phe19, Phe20, and Glu22 in the CHC region (β1-sheet) and Ile31, Leu34, Val36, and Val39 in the CT region (β2-sheet). For those CQ_2−*x* and CQ_3−*x* complexes, the cavity is also composed of the residues of Tyr10, His13, His14, and Val12 in the NT region. In addition, the electrostatic contribution to the binding energy of these CQ_2−*x* and CQ_3−*x* complexes also plays an important role. In a word, CQ_i can hinder aggregation only by binding to the Aβ rather than Cu^{2+} after a stable Aβ−Cu^{2+} complex has been generated. In a Cu^{2+} abundant or Cu^{2+}/Aβ coexisting system, CQ_i and Aβ would be competitive or work together to chelate Cu^{2+}.[24]

Interesting structure−activity relationships of these complexes were obtained qualitatively by comparing present results with the previous, and therefore three inhibition/disaggregation mechanisms were suggested for not only the present CQ_i drugs but also the others. If a drug molecule can insert inside of Aβ_{40} or its aggregates and form coated-structures, like CQ_2 in CQ_2−1 and CQ_1 in CQ_1−2, as well as NQTrp in Aβ_{42} dimer,[19,20] then the contact number between the drug and the ambient residues will be large and the corresponding binding would be strong, more than 100 kJ/mol generally. Then such binding mechanism is termed as "insertion mechanism". The binding strength of −143.1 to −203.4 kJ/mol between substrates 1EC2, 1D4H, and 1EZB and the hydrophobic cavity of HIV[47] should be attributed to such structure−activity relationship and "insertion mechanism". If a drug just inserts inside of Aβ partly or only attaches on the surface of Aβ or its aggregates, the binding strength and inhibitory effect would be generally weaker. We would term such interaction mechanisms as "semi-insertion mechanism" and "surface mechanism", respectively. In the present study, the interaction between CQ_3 and model 2 (−83.0 kJ/mol) was attributed to the semi-insertion mechanism and that between CQ_1 and model 1 (−65.6 kJ/mol) to the surface mechanism. Other inhibitor molecules involving such examples include natural polyphenols EGCG (−25.9 kJ/mol),[17,18,61] Aβ segment KLVFF (−29.7 kJ/mol) and its derivative LPFFD (−54.8 kJ/mol),[15] curcumin (−80.3 kJ/mol), naphthol (−36.4 kJ/mol), and ibuprofen (−13.3 kJ/mol).[67] Three possible binding modes between Wgx-50 and Aβ_{42} hexamer proposed by Fan et al. match well with the three mechanisms.[80] Therefore, strong binding was a key indicator for drug/inhibitor choice. Meanwhile H-bond generated between a drug and the Asp23 residue would play a key role because of its special effect on the salt-bridge Asp23−Lys28 formation and stability. Once such a H-bond is formed, inhibition/disaggregation effect would be prominent even although the binding between the drug (i.e., CQ_3) and Aβ is not the strongest. In addition, the drug polarity and the environment (i.e., pH) are also important factors that need to be considered. The drug with strong binding to the NT region rather than other regions would be the prior choice in alleviating the Aβ aggregation induced by Cu^{2+}.

The stronger insertion ability of CQ_i comes from not only the strong interaction between itself and Aβ_{40} chain but also from the flexible rotation ability of the C7−N14 bond. The rotation adjusts the orientations of both phenol and benzothiazole rings to match the surrounding Aβ chains and achieve the maximum insertion and affinity effects. Therefore, the structural flexibility should be adequately considered and utilized when a new drug is chosen and designed.

DOI: 10.1021/acschemneuro.5b00343
ACS Chem. Neurosci. 2016, 7, 599−614

Given that low molecular weight oligomers are more neurotoxic,[59] present results have great significance in understanding not only the mechanisms of both CQ_i inhibition/disaggregation and S1 → S2 transition but also the associated pathogenesis in AD induced by a Cu^{2+} binding. Most importantly, these results point the way to what structural characteristics of a drug would be more effective to inhibit the protein aggregation induced by Cu^{2+}.

■ ASSOCIATED CONTENT

Supporting Information

The Supporting Information is available free of charge on the ACS Publications website at DOI: 10.1021/acschemneuro.5b00343.

Topology files of model *x* and CQ_i (Tables S1−S6), binding energies between CQ_i and three Cu^{2+}−Aβ_{40} monomers by docking (Table S7), docked geometries of the three CQ_i in three model *x* complexes (Figure S1), equilibrium structures of Aβ_{40} monomer and model *x* (Figure S2), secondary structures of each residue in Aβ_{40} monomer, model *x*, and CQ_i−*x* complexes (Figures S3−S7) (PDF)

Movies S1−S9 (ZIP)

■ AUTHOR INFORMATION

Corresponding Author

*Hongqi Ai. E-mail: chm_aihq@ujn.edu.cn.

Funding

This work is supported by National Natural Science Foundation of China (NSFC) (Nos. 20973084 and 21211140340)

Notes

The authors declare no competing financial interest.

■ REFERENCES

(1) Goedert, M., and Spillantini, M. G. (2006) A century of Alzheimer's disease. *Science 314*, 777−781.

(2) Andreini, C., Bertini, I., Cavallaro, G., Holliday, G. L., and Thornton, J. M. (2008) Metal ions in biological catalysis: from enzyme databases to general principles. *J. Biol. Inorg. Chem. 13*, 1205−1218.

(3) Selkoe, D. J. (2001) Alzheimer's disease: genes, proteins, and therapy. *Physiol. Rev. 81*, 741−766.

(4) Dahlgren, K. N., Manelli, A. M., Stine, W. B., Baker, L. K., Krafft, G. A., and Ladu, M. J. (2002) Oligomeric and Fibrillar Species of Amyloid-β Peptides Differentially Affect Neuronal Viability. *J. Biol. Chem. 277*, 32046−32053.

(5) Lovell, M. A., Robertson, J. D., Teesdale, W. J., Campbell, J. L., and Markesbery, W. R. (1998) Copper, iron and zinc in Alzheimer's disease senile plaques. *J. Neurol. Sci. 158*, 47−52.

(6) Parthasarathy, S., Long, F., Miller, Y., Xiao, Y., McElheny, D., Thurber, K., Ma, B., Nussinov, R., and Ishii, Y. (2011) Molecular-Level Examination of Cu^{2+} Binding Structure for Amyloid Fibrils of 40-Residue Alzheimer's β by Solid-State NMR Spectroscopy. *J. Am. Chem. Soc. 133*, 3390−3400.

(7) Wise-Scira, O., Xu, L., Perry, G., and Coskuner, O. (2012) Structures and free energy landscapes of aqueous zinc(II)-bound amyloid-β(1−40) and zinc(II)-bound amyloid-β(1−42) with dynamics. *J. Biol. Inorg. Chem. 17*, 927−938.

(8) Curtain, C. C., Ali, F., Volitakis, I., Cherny, R. A., Norton, R. S., Beyreuther, K., Barrow, C. J., Masters, C. L., Bush, A. I., and Barnham, K. J. (2001) Alzheimer's Disease Amyloid-β Binds Copper and Zinc to Generate an Allosterically Ordered Membrane-penetrating Structure Containing Superoxide Dismutase-like Subunits. *J. Biol. Chem. 276*, 20466−20473.

(9) Drew, S. C., Masters, C. L., and Barnham, K. J. (2009) Alanine-2 Carbonyl is an Oxygen Ligand in Cu^{2+} Coordination of Alzheimer's Disease Amyloid-β Peptide − Relevance to N-Terminally Truncated Forms. *J. Am. Chem. Soc. 131*, 8760−8761.

(10) Alí-Torres, J., Maréchal, J.-D., Rodríguez-Santiago, L., and Sodupe, M. (2011) Three Dimensional Models of Cu^{2+}−Aβ(1−16) Complexes from Computational Approaches. *J. Am. Chem. Soc. 133*, 15008−15014.

(11) Drew, S. C., Noble, C. J., Masters, C. L., Hanson, G. R., and Barnham, K. J. (2009) Pleomorphic Copper Coordination by Alzheimer's Disease Amyloid-β Peptide. *J. Am. Chem. Soc. 131*, 1195−1207.

(12) Hureau, C., Coppel, Y., Dorlet, P., Solari, P. L., Sayen, S., Guillon, E., Sabater, L., and Faller, P. (2009) Deprotonation of the Asp1 Ala2 Peptide Bond Induces Modification of the Dynamic Copper(II) Environment in the Amyloid-β Peptide near Physiological pH. *Angew. Chem. 121*, 9686−9689.

(13) Alí-Torres, J., Mirats, A., Maréchal, J. D., Rodríguez-Santiago, L., and Sodupe, M. (2014) 3D structures and redox potentials of Cu^{2+}−Aβ(1−16) complexes at different pH: a computational study. *J. Phys. Chem. B 118*, 4840−4850.

(14) Tycko, R. (2011) Solid-State NMR Studies of Amyloid Fibril Structure. *Annu. Rev. Phys. Chem. 62*, 279−299.

(15) Takahashi, T., and Mihara, H. (2008) Peptide and protein mimetics inhibiting amyloid beta-peptide aggregation. *Acc. Chem. Res. 41*, 1309−1318.

(16) Viet, M. H., Ngo, S. T., Lam, N. S., and Li, M. S. (2011) Inhibition of Aggregation of Amyloid Peptides by Beta-Sheet Breaker Peptides and Their Binding Affinity. *J. Phys. Chem. B 115*, 7433−7446.

(17) Ehrnhoefer, D. E., Bieschke, J., Boeddrich, A., Herbst, M., Masino, L., Lurz, R., Engemann, S., Pastore, A., and Wanker, E. E. (2008) EGCG redirects amyloidogenic polypeptides into unstructured, off-pathway oligomers. *Nat. Struct. Mol. Biol. 15*, 558−566.

(18) Zhang, T., Zhang, J., Derreumaux, P., and Mu, Y. (2013) Molecular Mechanism of the Inhibition of EGCG on the Alzheimer Aβ1−42 Dimer. *J. Phys. Chem. B 117*, 3993−4002.

(19) Scherzer-Attali, R., Pellarin, R., Convertino, M., Frydman-Marom, A., Egoz-Matia, N., Peled, S., Levy-Sakin, M., Shalev, D. E., Caflisch, A., Gazit, E., and Segal, D. (2010) Complete Phenotypic Recovery of an Alzheimer's Disease Model by a Quinone-Tryptophan Hybrid Aggregation Inhibitor. *PLoS One 5*, e11101.

(20) Zhang, T., Xu, W., Mu, Y., and Derreumaux, P. (2014) Atomic and Dynamic Insights into the Beneficial Effect of the 1,4-Naphthoquinon-2-yl-l-tryptophan Inhibitor on Alzheimer's Aβ1−42 Dimer in Terms of Aggregation and Toxicity. *ACS Chem. Neurosci. 5*, 148−159.

(21) Cherny, R. A., Atwood, C. S., Xilinas, M. E., Gray, D. N., Jones, W. D., McLean, C. A., Barnham, K. J., Volitakis, I., Fraser, F. W., Kim, Y.-S., Huang, X., Goldstein, L. E., Moir, R. D., Lim, J. T., Beyreuther, K., Zheng, H., Tanzi, R. E., Masters, C. L., and Bush, A. I. (2001) Treatment with a Copper-Zinc Chelator Markedly and Rapidly Inhibits β-Amyloid Accumulation in Alzheimer's Disease Transgenic Mice. *Neuron 30*, 665−676.

(22) Li, M., Liu, Z., Ren, J., and Qu, X. (2012) Inhibition of metal-induced amyloid aggregation using light-responsive magnetic nanoparticle prochelator conjugates. *Chem. Sci. 3*, 868−873.

(23) Ono, M. H. S., Kimura, H., Kawashima, H., Nakayama, M., Saji, H., and Hayashi, S. (2009) Push−pull benzothiazole derivatives as probes for detecting beta-amyloid plaques in Alzheimer's brains. *Bioorg. Med. Chem. 17*, 7002−7007.

(24) Geng, J., Li, M., Wu, L., Ren, J., and Qu, X. (2012) Liberation of Copper from Amyloid Plaques: Making a Risk Factor Useful for Alzheimer's Disease Treatment. *J. Med. Chem. 55*, 9146−9155.

(25) Wu, C., Pike, V. W., and Wang, Y. (2005) Amyloid imaging: from benchtop to bedside. *Curr. Top. Dev. Biol. 70*, 171−213.

(26) Pardridge, W. M. (2009) Alzheimer's disease drug development and the problem of the blood−brain barrier. *Alzheimer's Dementia 5*, 427−432.

DOI: 10.1021/acschemneuro.5b00343
ACS Chem. Neurosci. 2016, 7, 599−614

(27) Clark, D. E., and Pickett, S. D. (2000) Computational methods for the prediction of 'drug-likeness'. *Drug Discovery Today 5*, 49−58.
(28) Petkova, A. T., Yau, W.-M., and Tycko, R. (2006) Experimental constraints on quaternary structure in Alzheimer's β-amyloid fibrils. *Biochemistry 45*, 498−512.
(29) Pettersen, E. F., Goddard, T. D., Huang, C. C., et al. (2004) UCSF Chimera – a visualization system for exploratory research and analysis. *J. Comput. Chem. 25*, 1605−1612.
(30) Becke, A. D. (1993) Density-functional thermochemistry. III. The role of exact exchange. *J. Chem. Phys. 98*, 5648−5652.
(31) Lee, C. T., Yang, W. T., and Parr, R. G. (1988) Development of the Colle-Salvetti correlation-energy formula into a functional of the electron density. *Phys. Rev. B: Condens. Matter Mater. Phys. 37*, 785−789.
(32) Frisch, M. J.; Trucks, G. W.; Schlegel, H. B.; Scuseria, G. E.; Robb, M. A.; Cheeseman, J. R.; Montgomery, J. A., Jr.; Vreven, T.; Kudin, K. N.; Burant, J. C.; Millam, J. M.; Iyengar, S. S.; Tomasi, J.; Barone, V.; Mennucci, B.; Cossi, M.; Scalmani, G.; Rega, N.; Petersson, G. A.; Nakatsuji, H.; Hada, M.; Ehara, M.; Toyota, K.; Fukuda, R.; Hasegawa, J.; Ishida, M.; Nakajima, T.; Honda, Y.; Kitao, O.; Nakai, H.; Klene, M.; Li, X.; Knox, J. E.; Hratchian, H. P.; Cross, J. B.; Bakken, V.; Adamo, C.; Jaramillo, J.; Gomperts, R.; Stratmann, R. E.; Yazyev, O.; Austin, A. J.; Cammi, R.; Pomelli, C.; Ochterski, J. W.; Ayala, P. Y.; Morokuma, K.; Voth, G. A.; Salvador, P.; Dannenberg, J. J.; Zakrzewski, V. G.; Dapprich, S.; Daniels, A. D.; Strain, M. C.; Farkas, O.; Malick, D. K.; Rabuck, A. D.; Raghavachari, K.; Foresman, J. B.; Ortiz, J. V.; Cui, Q.; Baboul, A. G.; Clifford, S.; Cioslowski, J.; Stefanov, B. B.; Liu, G.; Liashenko, A.; Piskorz, P.; Komaromi, I.; Martin, R. L.; Fox, D. J.; Keith, T.; Al-Laham, M. A.; Peng, C. Y.; Nanayakkara, A.; Challacombe, M.; Gill, P. M. W.; Johnson, B.; Chen, W.; Wong, M. W.; Gonzalez, C.; and Pople, J. A.(2003) *Gaussian 03*; Gaussian, Inc., Wallingford, CT.
(33) Peters, M. B., Yang, Y., Wang, B., Fusti-Molnar, L., Weaver, M. N., and Merz, K. M., Jr. (2010) Structural Survey of Zinc Containing Proteins and the Development of the Zinc AMBER Force Field (ZAFF). *J. Chem. Theory Comput. 6*, 2935−2947.
(34) Zhao, Y., Schultz, N. E., and Truhlar, D. G. (2006) Design of Density Functionals by Combining the Method of Constraint Satisfaction with Parametrization for Thermochemistry, Thermochemical Kinetics, and Noncovalent Interactions. *J. Chem. Theory Comput. 2*, 364−382.
(35) Hohenstein, E. G., Chill, S. T., and Sherrill, C. D. (2008) Assessment of the Performance of the M05-2X and M06-2X Exchange-Correlation Functionals for Noncovalent Interactions in Biomolecules. *J. Chem. Theory Comput. 4*, 1996−2000.
(36) Wang, J., Wolf, R. M., Caldwell, J. W., Kollman, P. A., and Case, D. A. (2004) Development and testing of a general AMBER force field. *J. Comput. Chem. 25*, 1157−1174.
(37) Morris, G. M., Huey, R., Lindstrom, W., Sanner, M. F., Belew, R. K., Goodsell, D. S., and Olson, A. J. (2009) AutoDock4 and AutoDockTools4: Automated docking with selective receptor flexibility. *J. Comput. Chem. 30*, 2785−2791.
(38) Morris, G. M., Goodsell, D. S., Halliday, R. S., et al. (1998) Automated docking using a Lamarckian genetic algorithm and an empirical binding free energy function. *J. Comput. Chem. 19*, 1639−1662.
(39) Zsoldos, Z., Reid, D., Simon, A., Sadjad, B. S., and Johnson, A. P. (2006) eHiTS: An Innovative Approach to the Docking and Scoring Function Problems. *Curr. Protein Pept. Sci. 7*, 421−435.
(40) Van Der Spoel, D., Lindahl, E., Hess, B., Groenhof, G., Mark, A. E., and Berendsen, H. J. C. (2005) GROMACS: Fast, flexible, and free. *J. Comput. Chem. 26*, 1701−1718.
(41) Lindorff-Larsen, K., Maragakis, P., Piana, S., Eastwood, M. P., Dror, R. O., and Shaw, D. E. (2012) Systematic Validation of Protein Force Fields against Experimental Data. *PLoS One 7*, e32131.
(42) Darden, T. A., York, D., and Pedersen, L. (1993) Particle mesh Ewald: an N•log(N) method for Ewald sums in large systems. *J. Chem. Phys. 98*, 10089.
(43) Hess, B., Bekker, H., Berendsen, H. J. C., and Fraaije, J. G. E. M. (1997) LINCS: a linear constraint solver for molecular simulations. *J. Comput. Chem. 18*, 1463−1472.
(44) Bussi, G., Donadio, D., and Parrinello, M. (2007) Canonical sampling through velocity rescaling. *J. Chem. Phys. 126*, 014101.
(45) Berendsen, H. J. C., Postma, J. P. M., van Gunsteren, W. F., DiNola, A., and Haak, J. R. (1984) Molecular dynamics with coupling to an external bath. *J. Chem. Phys. 81*, 3684−3690.
(46) Kabsch, W., and Sander, C. (1983) Dictionary of protein secondary structure: Pattern recognition of hydrogen-bonded and geometrical features. *Biopolymers 22*, 2577−2637.
(47) Zhou, X., Xi, W., Luo, Y., Cao, S., and Wei, G. (2014) Interactions of a Water-Soluble Fullerene Derivative with Amyloid-β Protofibrils: Dynamics, Binding Mechanism, and the Resulting Salt-Bridge Disruption. *J. Phys. Chem. B 118*, 6733−6741.
(48) Humphrey, W., Dalke, A., and Schulten, K. (1996) VMD: Visual modelcular dynamics. *J. Mol. Graphics 14*, 33.
(49) Baker, N. A., Sept, D., Joseph, S., Holst, M. J., and McCammon, J. A. (2001) Electrostatics of nanosystems: Application to microtubules and the ribosome. *Proc. Natl. Acad. Sci. U. S. A. 98*, 10037−10041.
(50) Kumari, R., Kumar, R., and Lynn, A. (2014) g_mmpbsa—A GROMACS Tool for High-Throughput MM-PBSA Calculations. *J. Chem. Inf. Model. 54*, 1951−1962.
(51) Onufriev, A., Bashford, D., and Case, D. A. (2000) Modification of the Generalized Born Model Suitable for Macromolecules. *J. Phys. Chem. B 104*, 3712−3720.
(52) Genheden, S., Kuhn, O., Mikulskis, P., Hoffmann, D., and Ryde, U. (2012) The Normal-Mode Entropy in the MM/GBSA Method: Effect of System Truncation, Buffer Region, and Dielectric Constant. *J. Chem. Inf. Model. 52*, 2079−2088.
(53) Hou, T., Wang, J., Li, Y., and Wang, W. (2011) Assessing the performance of the MM/PBSA and MM/GBSA methods: I. The accuracy of binding free energy calculations based on molecular dynamics simulations. *J. Chem. Inf. Model. 51*, 69−82.
(54) Khandogin, J., and Brooks, C. L., III (2007) Linking folding with aggregation in Alzheimer's beta-amyloid peptides. *Proc. Natl. Acad. Sci. U. S. A. 104*, 16880−16885.
(55) Cerdà-Costa, N., Esteras-Chopo, A., Avilés, F. X., Serrano, L., and Villegas, V. (2007) Early Kinetics of Amyloid Fibril Formation Reveals Conformational Reorganisation of Initial Aggregates. *J. Mol. Biol. 366*, 1351−1363.
(56) Sticht, H., Bayer, P., Willbold, D., Dames, S., Hilbich, C., Beyreuther, K., Frank, R. W., and Rösch, P. (1995) Structure of Amyloid A4-(1−40)-Peptide of Alzheimer's Disease. *Eur. J. Biochem. 233*, 293−298.
(57) Coles, M., Bicknell, W., Watson, A. A., Fairlie, D. P., and Craik, D. J. (1998) Solution Structure of Amyloid β-Peptide(1−40) in a Water−Micelle Environment. Is the Membrane-Spanning Domain Where We Think It Is? *Biochemistry 37*, 11064−11077.
(58) Rojas, A., Liwo, A., Browne, D., and Scheraga, H. A. (2010) Mechanism of fiber assembly: treatment of Aβ peptide aggregation with a coarse-grained united-residue force field. *J. Mol. Biol. 404*, 537−552.
(59) Vitalis, A., and Caflisch, A. (2010) Micelle-Like Architecture of the Monomer Ensemble of Alzheimer's Amyloid-β Peptide in Aqueous Solution and Its Implications for Aβ Aggregation. *J. Mol. Biol. 403*, 148−165.
(60) Fezoui, Y., and Teplow, D. B. (2002) Kinetic Studies of Amyloid β-Protein Fibril Assembly. *J. Biol. Chem. 277*, 36948−36954.
(61) Liu, F.-F., Dong, X.-Y., He, L., Middelberg, A. P. J., and Sun, Y. (2011) Molecular Insight into Conformational Transition of Amyloid β-Peptide 42 Inhibited by (−)-Epigallocatechin-3-gallate Probed by Molecular Simulations. *J. Phys. Chem. B 115*, 11879−11887.
(62) Somavarapu, A. K., and Kepp, K. P. (2015) Direct Correlation of Cell Toxicity to Conformational Ensembles of Genetic Aβ Variants. *ACS Chem. Neurosci. 6*, 1990.

DOI: 10.1021/acschemneuro.5b00343
ACS Chem. Neurosci. 2016, 7, 599−614

(63) Sørensen, J., Periole, X., Skeby, K. K., Marrink, S.-J., and Schiøtt, B. (2011) Protofibrillar Assembly Toward the Formation of Amyloid Fibrils. *J. Phys. Chem. Lett. 2*, 2385−2390.
(64) Qi, R., Luo, Y., Wei, G., Nussinov, R., and Ma, B. (2015) Aβ "Stretching-and-Packing" Cross-Seeding Mechanism Can Trigger Tau Protein Aggregation. *J. Phys. Chem. Lett. 6*, 3276−3282.
(65) Wang, Q., Ning, L., Niu, Y., Liu, H., and Yao, X. (2015) Molecular Mechanism of the Inhibition and Remodeling of Human Islet Amyloid Polypeptide (hIAPP1−37) Oligomer by Resveratrol from Molecular Dynamics Simulation. *J. Phys. Chem. B 119*, 15−24.
(66) Cairo, C. W., Strzelec, A., Murphy, R. M., and Kiessling, L. L. (2002) Affinity-Based Inhibition of β-Amyloid Toxicity. *Biochemistry 41*, 8620−8629.
(67) Ngo, S. T., and Li, M. S. (2012) Curcumin Binds to Aβ1−40 Peptides and Fibrils Stronger Than Ibuprofen and Naproxen. *J. Phys. Chem. B 116*, 10165−10175.
(68) Hong, L., Carducci, T. M., Bush, W. D., Dudzik, C. G., Millhauser, G. L., and Simon, J. D. (2010) Quantification of the Binding Properties of Cu^{2+} to the Amyloid Beta Peptide: Coordination Spheres for Human and Rat Peptides and Implication on Cu^{2+}-Induced Aggregation. *J. Phys. Chem. B 114*, 11261−11271.
(69) Silva, K. I., Michael, B. C., Geib, S. J., and Saxena, S. (2014) ESEEM analysis of multi-histidine Cu(II)-coordination in model complexes, peptides, and amyloid-β. *J. Phys. Chem. B 118*, 8935−8944.
(70) Gunderson, W. A., Hernández-Guzmán, J., Karr, J. W., Sun, L., Szalai, V. A., and Warncke, K. (2012) Local Structure and Global Patterning of Cu^{2+} Binding in Fibrillar Amyloid-β [Aβ(1−40)] Protein. *J. Am. Chem. Soc. 134*, 18330−18337.
(71) Alies, B., Eury, H., Bijani, C., Rechignat, L., Faller, P., and Hureau, C. (2011) pH-Dependent Cu(II) coordination to amyloid-β peptide: impact of sequence alterations, including the H6R and D7N familial mutations. *Inorg. Chem. 50*, 11192.
(72) Ngo, S., and Guo, Z. (2011) Key residues for the oligomerization of Aβ42 protein in Alzheimer's disease. *Biochem. Biophys. Res. Commun. 414*, 512−516.
(73) Lemkul, J. A., and Bevan, D. R. (2010) Assessing the Stability of Alzheimer's Amyloid Protofibrils Using Molecular Dynamics. *J. Phys. Chem. B 114*, 1652−1660.
(74) Ahmed, M., Davis, J., Aucoin, D., Sato, T., Ahuja, S., Aimoto, S., Elliott, J. I., Van Nostrand, W. E., and Smith, S. O. (2010) Structural conversion of neurotoxic amyloid-beta(1−42) oligomers to fibrils. *Nat. Struct. Mol. Biol. 17*, 561−567.
(75) Sinha, S., et al. (2012) A Key Role for Lysine&10;Residues in Amyloid β-Protein&10;Folding, Assembly, and Toxicity. *ACS Chem. Neurosci. 3*, 473.
(76) Kaden, D., Harmeier, A., Weise, C., Munter, L. M., Althoff, V., Rost, B. R., Hildebrand, P. W., Schmitz, D., Schaefer, M., Lurz, R., et al. (2012) Novel APP/Aβ mutation K16N produces highly toxic heteromeric Aβ oligomers. *EMBO Mol. Med. 4*, 647−659.
(77) Zhang, S., Iwata, K., Lachenmann, M. J., Peng, J. W., Li, S., Stimson, E. R., Lu, Y. A., Felix, A. M., Maggio, J. E., and Lee, J. P. (2000) The Alzheimer's Peptide Aβ Adopts a Collapsed Coil Structure in Water. *J. Struct. Biol. 130*, 130−141.
(78) Zhang, S., Casey, N., and Lee, J. P. (1998) Residual structure in the Alzheimer's disease peptide: probing the origin of a central hydrophobic cluster. *Folding Des. 3*, 413−422.
(79) Dobson, C. M. (2006) Protein aggregation and its consequences for human disease. *Protein Pept. Lett. 13*, 219−227.
(80) Fan, H.-M., Gu, R.-X., Wang, Y.-J., Pi, Y.-L., Zhang, Y.-H., Xu, Q., and Wei, D.-Q. (2015) Destabilization of Alzheimer's Aβ42 Protofibrils with a Novel Drug Candidate wgx-50 by Molecular Dynamics Simulations. *J. Phys. Chem. B 119*, 11196−11202.

DOI: 10.1021/acschemneuro.5b00343
ACS Chem. Neurosci. 2016, 7, 599−614